

Resummed jet mass distribution with trimming in Z+jet events at the LHC

Safa Gaid,^a Yazid Delenda^{a,1} and Rachik Soualah^{b,c}

^a*Laboratoire de Physique des Rayonnements et de leurs Interactions avec la Matière,
Département de Physique, Faculté des Sciences de la Matière, Université de Batna-1,
Batna 05000, Algeria*

^b*Department of Physics, Khalifa University of Science and Technology,
P.O. Box 127788, Abu Dhabi, United Arab Emirates*

^c*The International Center for Theoretical Physics (ICTP),
Strada Costiera 11, Trieste I-34151, Italy*

E-mail: safa.gaid@univ-batna.dz, yazid.delenda@univ-batna.dz,
rachik.soualah@ku.ac.ae

ABSTRACT: In this paper, we calculate the resummed jet mass distribution up to next-to-leading logarithmic accuracy for jets defined with the trimming groomer in Z+jet events at the LHC. We compute at fixed order and to all orders the large logarithms, both in the jet mass and z_{cut} trimming variable, including non-global and clustering logarithms. We conduct phenomenological studies at $\mathcal{O}(\alpha_s)$, validating our results by comparing them with the fixed-order Monte Carlo program MCFM, which provides NLO predictions for hadron colliders. The resummation of non-global logarithms is estimated in the large- N_c limit. Our resummed result is compared to Monte Carlo parton shower simulations from Pythia 8, Herwig ++ and Sherpa 2 event generators.

KEYWORDS: Jets and Jet Substructure, Resummation

¹Corresponding author.

Contents

1	Introduction	1
2	Jet mass distribution	3
2.1	Process kinematics	3
2.2	Jet mass, clustering algorithms, and grooming	4
2.3	Resummed trimmed jet mass distribution and global form factor	5
3	The jet mass distribution at leading order with trimming	6
3.1	Review of the ungroomed distribution	6
3.2	Trimming correction at leading order	7
3.3	Comparison to Monte Carlo results	9
3.4	NLL' corrections	11
4	Two-loop calculation: NGLs and CLs	11
4.1	Ungroomed NGLs with anti- k_t and k_t clustering	11
4.2	Trimmed NGLs	13
4.3	Ungroomed CLs with k_t clustering	14
4.4	Trimmed CLs	15
4.5	NGLs at all orders	17
5	Convolution and numerical results	19
6	Conclusions	21
A	Radiator	22
B	Clustering functions	24

1 Introduction

Jets are copiously produced at the CERN-Large Hadron Collider (LHC), predominantly arising from the hard QCD dynamics of partons and their associated soft emissions, as well as contributions from the underlying event and pileup interactions which further complicate the jet environment. Jets also emerge from the hadronic decay products of heavy particles, particularly top quarks, weak bosons, and the Higgs boson - particles that are key targets of study at collider experiments. Moreover, potential new physics signals, such as Dark Matter candidates from different physics scenarios, might also decay into jets. The decay products of a heavy particle with mass M and transverse momentum p_t typically cluster

within a radius of $R \sim 2M/p_t$. In the extreme regions of phase space reached by the high-energy proton-proton collisions at the LHC, these heavy particles can acquire significant Lorentz boosts, leading to collimated decay products that eventually manifest as a single large-radius fat jet.

Distinguishing such electroweak signal events from the overwhelming QCD background is a major challenge. Jet substructure techniques have emerged as powerful tools to address this, enabling more precise discrimination between different types of jets [1–4]. These jet grooming techniques selectively remove soft wide-angle radiation within jets that is less likely to have originated from the hard parton that initiated the jet, thereby enabling more accurate and cleaner studies of jet properties. Consequently, jet grooming has proven invaluable in mitigating contamination from pileup interactions and the underlying event, a capability that will be crucial as the LHC moves towards its High-Luminosity phase (HL-LHC).

The application of jet substructure techniques is widespread, extending to various new physics searches conducted by the CMS and ATLAS experiments at the LHC — see for example refs. [5–7]. Beyond searches for new physics, these techniques have demonstrated promise for precision QCD measurements, such as determining the strong coupling constant α_s [8, 9]. Popular grooming algorithms include trimming [10], pruning [11, 12], filtering/mass drop tagger (MDT) [13], modified MDT (mMDT) [14], and soft drop [15]. Comprehensive reviews on jet substructure can be found in refs. [16–18].

Among the various observables used in these studies, the invariant mass of the jet stands out as particularly important. The jet mass plays a crucial role in the said disentanglement of electroweak signals from QCD backgrounds and provides insight into perturbative and non-perturbative QCD dynamics. Both the ATLAS and CMS collaborations have conducted experimental studies on the groomed jet mass distribution in a variety of final states, such as dijet events, single jets associated with a vector boson, and boosted W/Z and top production [19–25].

The jet mass observable has attracted substantial interest due to its sensitivity to various QCD dynamics. The distribution of this observable is characterized by large logarithms of the ratio of the jet mass m_j to its transverse momentum p_t . At next-to-leading logarithmic (NLL) accuracy, all the leading logarithms $\alpha_s^n \ln^{n+1}(m_j/p_t)$ and next-to-leading logarithms $\alpha_s^n \ln^n(m_j/p_t)$ in the exponent of the cumulative distribution are resummed to all orders. Studies on the jet mass distribution for ungroomed jets using anti- k_t [26] and k_t [27, 28] clustering in vector-boson+jet final states have been conducted in refs. [29, 30]. Additionally, the first analytical calculations of the jet mass distribution using various substructure methods were performed in refs. [14, 31] for the e^+e^- annihilation to dijets.

A significant focus of theoretical study has been on Non-Global Logarithms (NGLs) [32, 33] and Clustering Logarithms (CLs) [34, 35], which appear in the jet mass spectrum for certain grooming algorithms. NGLs arise from the correlated emission of soft gluons, while CLs originate from primary emissions directly from the hard partons. Resumming these logarithms to all orders is complex and often requires numerical Monte Carlo approaches in the large- N_c approximation, where N_c is the number of QCD quark colors. These logarithms are present in the jet mass distribution for groomers like trimming and pruning but are

absent in others, such as mMDT [14, 31]. As a result, this has led to the popularity of the mMDT algorithm in jet mass studies [36–42], as it simplifies resummation to NNLL accuracy (and perhaps beyond) using either the soft collinear effective theory (SCET) approach or ordinary QCD perturbation theory.

In this paper, we focus on the NLL resummation of the jet mass distribution in Z +jet final states at the LHC proton-proton collisions for jets defined using the trimming algorithm. This groomer, frequently used by the ATLAS experiment, presents unique challenges, particularly in dealing with the emergence of NGLs and CLs. We perform a fixed-order calculation of the trimmed distribution at leading order and compare our results with those obtained from the Monte Carlo program MCFM 9.1 [43], finding agreement. By subtracting the large logarithms from the MCFM distribution, the resulting constant at small jet mass values is used to extend the accuracy of the perturbative jet mass distribution to NLL’, accounting for all logarithms of the form $\alpha_s^n \ln^m(m_j/p_t)$, with $m = \{2n, 2n - 1, 2n - 2\}$ in the order-by-order expansion of the cumulative distribution [44].

At next-to-leading order ($\mathcal{O}(\alpha_s^2)$), we calculate the contributions of NGLs and CLs to the trimmed distribution and assess their impact. While CLs are negligible, NGLs remain moderate. We then use a Monte Carlo program [32, 33] to resum the NGLs at leading-color approximation. Next, we perform a numerical convolution of the resummed global and non-global form factors with the Born cross-section using the MadGraph5_aMC@NLO [45, 46] event generator. Our numerical results for the NLL distribution, with and without trimming, are presented, highlighting the impact of trimming on the distribution. Finally, we compare the resummed results with parton shower simulations from Pythia 8.3 [47, 48], Herwig ++ [49, 50], and Sherpa 2.2 [51].

This paper is organized as follows. In Section 2, we define the kinematics of the process $pp \rightarrow Z$ +jet and introduce the jet mass observable. We also provide a brief review of the clustering algorithms used and present the general expression for the jet mass distribution as a convolution of the Born cross-section with the resummed global and non-global form factors. In Section 3, we perform a fixed-order calculation of this distribution and compare the results with those obtained using MCFM. In Section 4, we calculate NGLs and CLs at $\mathcal{O}(\alpha_s^2)$ and resum the NGLs to all orders. Section 5 presents our numerical results, comparing them to various simulations of Monte Carlo event generators. Finally, in Section 6, we summarize our findings and conclusions. The notations from refs. [29, 30, 52] are used throughout this paper.

2 Jet mass distribution

2.1 Process kinematics

We examine the process of production of a Z boson and a hard jet in pp collisions at a center-of-mass energy \sqrt{s} . The Z plus jet final state has garnered significant interest due to its crucial role in various phenomenological studies. These include its presence as an important background in many processes, its clean experimental signature from Z decays, and its use in probing parton distribution functions and the strong coupling constant. One

notable example of such studies is the application of the Transverse Momentum Dependent (TMD) resummation formalism to some observable distributions in this process [53].

To achieve Single Logarithmic (SL) accuracy in resummation, we assume the emitted gluons are strongly ordered in transverse momentum k_{ti} , such that at the n^{th} order: $k_{tn} \ll \dots \ll k_{t2} \ll k_{t1} \ll p_t$, where p_t is the jet's transverse momentum. In this regime, the momenta of the incoming partons (a) and (b), carrying momentum fractions x_a and x_b of the colliding protons, along with the outgoing hard parton (j) and soft emissions (i), are expressed as:

$$p_a = x_a \frac{\sqrt{s}}{2} (1, 0, 0, 1), \quad (2.1a)$$

$$p_b = x_b \frac{\sqrt{s}}{2} (1, 0, 0, -1), \quad (2.1b)$$

$$p_j = p_t (\cosh y, \cos \varphi, \sin \varphi, \sinh y), \quad (2.1c)$$

$$k_i = k_{ti} (\cosh \eta_i, \cos \phi_i, \sin \phi_i, \sinh \eta_i), \quad (2.1d)$$

where y and η_i are the rapidities of the jet and soft emissions, and φ and ϕ_i are their respective azimuthal angles, measured relative to the beam axis. Neglecting recoil effects is justified at SL accuracy.

We use polar coordinates (r, θ) in the $\eta - \phi$ plane, centered at the jet-initiating parton (y, φ) . Each particle k_i is characterized by r_i and θ_i

$$\eta_i - y = R r_i \cos \theta_i, \quad (2.2a)$$

$$\phi_i - \varphi = R r_i \sin \theta_i, \quad (2.2b)$$

where r_i is normalized to the jet radius R , so that $r_i = 1$ corresponds to the jet boundary.

At Born level, the two relevant partonic subprocesses for Z boson and jet production in pp collisions are $(\delta_g): q\bar{q} \rightarrow Zg$ and $(\delta_q): qg \rightarrow Zq$. The subscripts q (for quarks/anti-quarks) and g (for gluons) indicate the nature of the outgoing parton initiating the jet.

2.2 Jet mass, clustering algorithms, and grooming

We study the normalized invariant jet mass (squared), defined as:

$$\rho = \frac{1}{p_t^2} \left(p_j + \sum_{i \in \text{jet}} k_i \right)^2, \quad (2.3)$$

where the sum includes all soft gluons within the jet. In the massless-quarks limit and under the strong ordering approximation (relevant for NLL resummation), this simplifies to

$$\begin{aligned} \rho &= \sum_{i \in \text{jet}} \frac{2 k_{ti}}{p_t} [\cosh(\eta_i - y) - \cos(\phi_i - \varphi)] \\ &\approx \sum_{i \in \text{jet}} \frac{k_{ti}}{p_t} R^2 r_i^2, \end{aligned} \quad (2.4)$$

with the final approximation valid at NLL accuracy.

Sequential recombination algorithms define two types of distances: between particle pairs d_{ij} and between particles and the beam d_{iB}

$$d_{ij} = \min(k_{ti}^{2p}, k_{tj}^{2p}) R_{ij}^2, \quad \text{with } R_{ij}^2 = (\eta_i - \eta_j)^2 + (\phi_i - \phi_j)^2, \quad (2.5a)$$

$$d_{iB} = k_{ti}^{2p} R^2, \quad (2.5b)$$

where R is the jet radius and p determines the clustering algorithm: $p = -1$ for anti- k_t [26], $p = +1$ for k_t [27, 28], and $p = 0$ for Cambridge-Aachen (CA) [54].

Several jet grooming techniques have been developed to improve jet substructure studies, including mass-drop/filtering [13], trimming [10], and pruning [11, 12]. In this work, we focus on trimming as described in ref. [10]. In summary, jets are clustered using a sequential recombination algorithm with a jet radius R . We use the anti- k_t algorithm with $R = 0.7$. The jet constituents are then re-clustered into sub-jets with a smaller radius R_{sub} . For this phase, we consider the k_t algorithm with $R_{\text{sub}} = 0.2$. Sub-jets with momentum fractions below a chosen threshold z_{cut} are removed. We set $z_{\text{cut}} = 0.03$. The final trimmed jet comprises all particles from the original jet, excluding those in rejected sub-jets. This trimming procedure is actually less aggressive than pruning but removes more particles than filtering.

2.3 Resummed trimmed jet mass distribution and global form factor

The integrated jet mass distribution is formulated as a sum over channels δ , involving a convolution of the differential cross-section $d\sigma_{0\delta}/d\mathcal{B}_\delta$ for the Born configuration \mathcal{B}_δ with the resummed global form factor $f_{\mathcal{B},\delta}(\rho)$, as well as the non-global and clustering functions $\mathcal{S}_\delta(\rho)$ and $\mathcal{C}_\delta(\rho)$ [52]

$$\sigma(\rho) = \sum_{\delta} \int d\mathcal{B}_\delta \frac{d\sigma_{0\delta}}{d\mathcal{B}_\delta} \Omega_{\mathcal{B}} f_{\mathcal{B},\delta}(\rho) \mathcal{S}_\delta(\rho) \mathcal{C}_\delta(\rho) (1 + \alpha_s C_1(\mathcal{B}_\delta) + \mathcal{O}(\alpha_s^2)), \quad (2.6)$$

where $\Omega_{\mathcal{B}}$ represents the experimental cuts and $C_1(\mathcal{B}_\delta)$ is the $\mathcal{O}(\alpha_s)$ correction term, introduced to improve the accuracy up to NLL'. A detailed discussion of this correction term will be provided later.

The global form factor is expressed in the form of an exponential function as follows

$$f_{\mathcal{B},\delta}(\rho) = \frac{1}{\Gamma[1 + \mathcal{R}'_\delta(\rho)]} \exp[-\mathcal{R}_\delta(\rho) - \gamma_E \mathcal{R}'_\delta(\rho)], \quad (2.7)$$

where \mathcal{R}_δ is the radiator associated with channel δ , γ_E is the Euler-Mascheroni constant, and $\mathcal{R}'_\delta(\rho)$ is the derivative of the radiator with respect to the resummed logarithms.

In the following section, we shall first compute the leading-order expansion in α_s of the form factor $f_{\mathcal{B},\delta}(\rho)$. The full expression of the radiator to NLL accuracy is provided in Appendix A. We shall then, in Section 4, derive the non-global and clustering corrections at second order in the coupling, and estimate their resummed result at all orders in the large- N_c approximation. The convolution in eq. (2.6) is then performed in Section 5. For now, we begin by evaluating $f_{\mathcal{B},\delta}^{(1)}(\rho)$, the leading-order expansion of the global form factor.

3 The jet mass distribution at leading order with trimming

3.1 Review of the ungroomed distribution

We begin by reviewing the ungroomed form factor at leading order, as computed in refs. [29, 30]. At first order in the strong coupling, the final state consists of a single soft gluon emission k_1 alongside the hard parton initiating the jet p_j . Within the strongly ordered regime, the gluon is clustered to the hard jet if its distance from the hard parton in the $\eta - \phi$ plane is actually less than R , $R_{1j} < R$. This leads to a non-zero jet mass for real emissions, while the jet mass remains zero in virtual corrections, resulting in a mis-cancellation of real and virtual soft-collinear singularities.

The form factor for channel δ , in the eikonal approximation (sufficient to capture the soft singularities), is given at $\mathcal{O}(\alpha_s)$ for a k_t , anti- k_t , or CA-clustered jet of radius R by [29, 30]

$$f_{\mathcal{B},\delta}^{\text{ungr},(1)}(\rho) = - \sum_{(i\ell)} \mathcal{C}_{i\ell} \frac{R^2}{2} \int \frac{d\xi_1}{\xi_1} dr_1^2 \frac{d\theta_1}{2\pi} \bar{\alpha}_s \omega_{i\ell}^1 \Theta(\xi_1 R^2 r_1^2 - \rho) \Xi_{\text{in}}^{\text{ungr}}(k_1), \quad (3.1)$$

where the sum is over the dipoles formed by the hard/eikonal legs $(i\ell) = \{(ab), (aj), (bj)\}$. The color factors, $\mathcal{C}_{i\ell}$, depend on the nature of the partons involved: $\mathcal{C}_{i\ell} = C_A = N_c$ for dipoles involving gluons and $\mathcal{C}_{i\ell} = 2C_F - C_A = -1/N_c$ for dipoles involving only quarks or anti-quarks. Here, $C_A = N_c$ and $C_F = (N_c^2 - 1)/(2N_c)$ are the QCD color factors with $N_c = 3$. The quantity $\xi_1 = k_{t1}/p_t$ is the momentum fraction of the soft emission relative to the jet's transverse momentum p_t . The angular antenna function for the emission of the soft gluon k_1 from the dipole $(i\ell)$ is given by

$$\omega_{i\ell}^1 = \frac{k_{t1}^2}{2} \frac{p_i \cdot p_\ell}{(p_i \cdot k_1)(k_1 \cdot p_\ell)}. \quad (3.2)$$

For the dipole (ab) , $\omega_{ab}^1 = 1$, and for dipoles (aj) and (bj) , we have

$$\omega_{aj}^1 = \frac{1}{2} \frac{\exp(R r_1 \cos \theta_1)}{\cosh(R r_1 \cos \theta_1) - \cos(R r_1 \sin \theta_1)}, \quad (3.3a)$$

$$\omega_{bj}^1 = \frac{1}{2} \frac{\exp(-R r_1 \cos \theta_1)}{\cosh(R r_1 \cos \theta_1) - \cos(R r_1 \sin \theta_1)}. \quad (3.3b)$$

In eq. (3.1), $\bar{\alpha}_s = \alpha_s/\pi$ is the “reduced” strong coupling. While its argument is irrelevant at leading order, for full resummation it is evaluated at the invariant transverse momentum of the emission k_1 in the emitting dipole's rest frame, $\kappa_{t1,(i\ell)}^2 = k_{t1}^2/\omega_{i\ell}^1$. For dipole (ab) , $\kappa_{t1,(ab)}^2 = k_{t1}^2 = \xi_1^2 p_t^2$, and for dipoles (aj) and (bj) at NLL accuracy, $\kappa_{t1,(aj)}^2 = k_{t1}^2 R^2 r_1^2 = \xi_1^2 p_t^2 R^2 r_1^2$.

The step function $\Theta(\xi_1 R^2 r_1^2 - \rho)$ ensures that in the integrated distribution, the jet mass (equal to $\xi_1 R^2 r_1^2$ at NLL accuracy) is less than ρ for real emissions. Only virtual emissions with $\xi_1 R^2 r_1^2 > \rho$ remain uncanceled and are integrated over. Lastly, $\Xi_{\text{in}}(k_1)$ restricts the integration region so that the gluon remains within the jet after clustering. For k_t , anti- k_t , and CA algorithms, it is simply given by

$$\Xi_{\text{in}}^{\text{ungr}}(k_1) = \Theta(R^2 - R_{1j}^2) = \Theta(1 - r_1^2), \quad (3.4)$$

where $R_{1j}^2 = R^2 r_1^2$.

After performing the integrations, and including corrections due to hard-collinear emissions to the outgoing jet, the NLL result is

$$f_{\mathcal{B},\delta}^{\text{ungr},(1)}(\rho) = - \left(C_j B_j + \sum_{(i\ell)} \mathcal{C}_{i\ell} \mathcal{J}_{i\ell}(R^2) \right) \bar{\alpha}_s \ln \frac{R^2}{\rho} - \frac{C_j}{2} \bar{\alpha}_s \ln^2 \frac{R^2}{\rho}, \quad (3.5)$$

where $C_j = (\mathcal{C}_{aj} + \mathcal{C}_{bj})/2$, with $C_j = C_F$ for quark-initiated jets and $C_j = C_A$ for gluon-initiated jets. The B_j term accounts for hard-collinear corrections, and we have

$$\begin{aligned} B_q &= -\frac{3}{4} && \text{quark-initiated jets,} \\ B_g &= -\frac{11 C_A - 4 T_R n_f}{12 C_A} = -\frac{\pi \beta_0}{C_A} && \text{gluons-initiated jets,} \end{aligned} \quad (3.6)$$

where $T_R = 1/2$ is the normalization constant for $SU(N_c)$, $n_f = 5$ is the number of active flavors, and β_0 is the one-loop coefficient of the QCD beta function. This correction arises from using the full splitting functions in the double logarithmic integration over energy fractions, where $1/\xi_1$ is replaced by $P_j(\xi_1)/\xi_1$ in the integrand. For a quark jet ($j = q$) and a gluon jet ($j = g$), the splitting functions, stripped of color factors, are given by [52]

$$P_q(\xi) = \xi P_{gq}(\xi), \quad (3.7a)$$

$$P_g(\xi) = \xi \frac{1}{2} P_{gg}(\xi) + \frac{T_R n_f}{C_A} \xi P_{qg}(\xi), \quad (3.7b)$$

where

$$P_{gq}(\xi) = \frac{1 + (1 - \xi)^2}{2\xi}, \quad (3.8a)$$

$$P_{gg}(\xi) = \frac{2(1 - \xi)}{\xi} + \xi(1 - \xi), \quad (3.8b)$$

$$P_{qg}(\xi) = \frac{1}{2} [\xi^2 + (1 - \xi)^2]. \quad (3.8c)$$

The jet functions $\mathcal{J}_{i\ell}$ are

$$\mathcal{J}_{ab}(R^2) = \frac{R^2}{2}, \quad (3.9a)$$

$$\mathcal{J}_{aj}(R^2) = \mathcal{J}_{bj}(R^2) = \frac{R^2}{8} + \frac{R^4}{576} + \frac{R^8}{4147200} + \mathcal{O}(R^{12}). \quad (3.9b)$$

These functions result from the angular integration over the dipole antenna functions and are expressed as a truncated series in the jet radius R . The truncation is sufficiently accurate for values of R up to order 1.

3.2 Trimming correction at leading order

Now, let us examine how trimming affects the jet mass distribution. When the soft gluon k_1 is emitted within a distance R_{sub} from the hard parton in the $\eta - \phi$ plane, it remains in

the jet after trimming. Additionally, if this gluon is emitted within an annulus defined by inner radius R_{sub} and outer radius R , and its transverse momentum satisfies $k_{t1} > z_{\text{cut}} p_t$, it forms a sub-jet that is retained alongside the hard sub-jet of the Born parton, contributing to the final jet mass. However, if $k_{t1} < z_{\text{cut}} p_t$, the sub-jet formed by the soft emission is trimmed away, yielding a zero jet mass. Furthermore, if the soft gluon is emitted at a distance greater than R from the hard parton, it does not get clustered into the jet, also resulting in a vanishing jet mass.

The leading-order form factor $f_{B,\delta}^{\text{trim},(1)}$ for trimmed jets is similar to the ungroomed jet mass form factor in eq. (3.1), with the replacement of the angular phase space $\Xi_{\text{in}}^{\text{ungr}}(k_1) \rightarrow \Xi_{\text{in}}^{\text{trim}}(k_1)$, ensuring that the gluon k_1 remains in the jet after trimming. The trimmed angular phase-space is given by

$$\Xi_{\text{in}}^{\text{trim}}(k_1) = \Theta(R_{\text{sub}}^2 - R_{1j}^2) + \Theta(R_{1j}^2 - R_{\text{sub}}^2) \Theta(R^2 - R_{1j}^2) \Theta(\xi_1 - z_{\text{cut}}). \quad (3.10)$$

Multiplying by the step function $\Theta(\xi_1 R_{1j}^2 - \rho) = \Theta(\xi_1 - \rho/R_{1j}^2)$, we express the phase space in a form that clearly defines the lower limit on the ξ_1 integration, depending on whether z_{cut} or ρ/R_{1j}^2 is smaller. We can then write

$$\begin{aligned} \Theta(\xi_1 R_{1j}^2 - \rho) \Xi_{\text{in}}^{\text{trim}} &= \Theta(\xi_1 R_{1j}^2 - \rho) \Theta(R_{\text{sub}}^2 - R_{1j}^2) \\ &\quad + \Theta(\xi_1 R_{1j}^2 - \rho) \Theta(R_{1j}^2 - R_{\text{sub}}^2) \Theta(R^2 - R_{1j}^2) \Theta(\rho/z_{\text{cut}} - R_{1j}^2) \\ &\quad + \Theta(\xi_1 - z_{\text{cut}}) \Theta(R_{1j}^2 - R_{\text{sub}}^2) \Theta(R^2 - R_{1j}^2) \Theta(R_{1j}^2 - \rho/z_{\text{cut}}). \end{aligned} \quad (3.11)$$

The second term in eq. (3.11) defines the integration region for the variable r_1 such that

$$R_{\text{sub}}^2 < R^2 r_1^2 < \min(R^2, \rho/z_{\text{cut}}), \quad (3.12)$$

which contributes only if $\rho > R_{\text{sub}}^2 z_{\text{cut}}$. Additionally, the third term in eq. (3.11) yields

$$\max(R_{\text{sub}}^2, \rho/z_{\text{cut}}) < R^2 r_1^2 < R^2, \quad (3.13)$$

which contributes only when $\rho < R^2 z_{\text{cut}}$.

We thus identify three distinct regions of the ρ variable with two transition points: a large- ρ region where $\rho > R^2 z_{\text{cut}}$, an intermediate region $R_{\text{sub}}^2 z_{\text{cut}} < \rho < R^2 z_{\text{cut}}$, and a small- ρ region where $\rho < R_{\text{sub}}^2 z_{\text{cut}}$. For the chosen values of R , R_{sub} , and z_{cut} , the transition points are $R^2 z_{\text{cut}} = 0.015$ and $R_{\text{sub}}^2 z_{\text{cut}} = 0.0012$. The phase space can be written in a compact form for each region as follows

- Large- ρ region, $\rho > R^2 z_{\text{cut}}$

$$\Theta(\xi_1 R_{1j}^2 - \rho) \Xi_{\text{in}}^{\text{trim}} = \Theta(\xi_1 R_{1j}^2 - \rho) \Theta(R^2 - R_{1j}^2). \quad (3.14)$$

- Intermediate- ρ region, $R_{\text{sub}}^2 z_{\text{cut}} < \rho < R^2 z_{\text{cut}}$

$$\begin{aligned} \Theta(\xi_1 R_{1j}^2 - \rho) \Xi_{\text{in}}^{\text{trim}} &= \Theta(\xi_1 R_{1j}^2 - \rho) \Theta(\rho/z_{\text{cut}} - R_{1j}^2) \\ &\quad + \Theta(\xi_1 - z_{\text{cut}}) \Theta(R^2 - R_{1j}^2) \Theta(R_{1j}^2 - \rho/z_{\text{cut}}). \end{aligned} \quad (3.15)$$

- Small- ρ region, $\rho < R_{\text{sub}}^2 z_{\text{cut}}$

$$\begin{aligned} \Theta(\xi_1 R_{1j}^2 - \rho) \Xi_{\text{in}}^{\text{trim}} &= \Theta(\xi_1 R_{1j}^2 - \rho) \Theta(R_{\text{sub}}^2 - R_{1j}^2) \\ &+ \Theta(\xi_1 - z_{\text{cut}}) \Theta(R^2 - R_{1j}^2) \Theta(R_{1j}^2 - R_{\text{sub}}^2). \end{aligned} \quad (3.16)$$

In the large- ρ region, the angular phase space for the trimmed jet mass form factor is identical to the ungroomed case. This implies that the distribution in this region, at NLL accuracy, is unaffected by trimming and follows the same form as eq. (3.5).

To integrate eq. (3.1) using the phase space in eq. (3.10), we expand the antenna functions as a power series in R . The result splits into collinear and wide-angle contributions as follows

$$f_{\mathcal{B},\delta}^{\text{trim},(1)}(\rho) = f_{\mathcal{B},\delta,\text{wide}}^{\text{trim},(1)}(\rho) + f_{\mathcal{B},\delta,\text{coll.}}^{\text{trim},(1)}(\rho), \quad (3.17)$$

with the collinear contribution containing double (soft collinear) logarithms and single (hard collinear) logarithms

$$\begin{aligned} f_{\mathcal{B},\delta,\text{coll.}}^{\text{trim},(1)}(\rho) &= -\frac{C_j}{2} \bar{\alpha}_s \ln^2 \min \left[\frac{R^2}{\rho}, \max \left(\frac{1}{z_{\text{cut}}}, \frac{R_{\text{sub}}^2}{\rho} \right) \right] - C_j B_j \bar{\alpha}_s \ln \frac{R^2}{\rho} \\ &- \Theta(R^2 z_{\text{cut}} - \rho) C_j \bar{\alpha}_s \ln \frac{1}{z_{\text{cut}}} \left[\ln \frac{R^2}{\rho} - \ln \max \left(\frac{1}{z_{\text{cut}}}, \frac{R_{\text{sub}}^2}{\rho} \right) \right], \end{aligned} \quad (3.18)$$

and the soft wide-angle contribution containing only single logarithms

$$\begin{aligned} f_{\mathcal{B},\delta,\text{wide}}^{\text{trim},(1)}(\rho) &= -\sum_{(i\ell)} C_{i\ell} \mathcal{J}_{i\ell} \left(\min [R^2, \max\{\rho/z_{\text{cut}}, R_{\text{sub}}^2\}] \right) \bar{\alpha}_s \ln \frac{R^2}{\rho} \\ &- \Theta(R^2 z_{\text{cut}} - \rho) \sum_{(i\ell)} C_{i\ell} [\mathcal{J}_{i\ell}(R^2) - \mathcal{J}_{i\ell}(\max[\rho/z_{\text{cut}}, R_{\text{sub}}^2])] \bar{\alpha}_s \ln \frac{1}{z_{\text{cut}}}. \end{aligned} \quad (3.19)$$

It is important to note that while the $\mathcal{O}(\rho/z_{\text{cut}})$ terms in the jet functions for the soft wide-angle contribution are formally sub-leading, they have a significant numerical impact in the region where $\rho \sim z_{\text{cut}}$ and therefore cannot be neglected.¹ These terms are also necessary to maintain the continuity of the distribution across the transition points. Our finding is consistent with the results obtained in ref. [14] for the trimmed jet mass distribution in e^+e^- annihilation to jets.

3.3 Comparison to Monte Carlo results

To validate our analytical results, we conduct a phenomenological study to compare them with Monte Carlo simulations. Figure 1 displays the analytical differential distribution $d\sigma/dL$, obtained by differentiating $\sigma(\rho)$ (using eq. (2.6) at $\mathcal{O}(\alpha_s)$) with respect to $L = \ln(R^2/\rho)$. This analytical distribution is compared to the Monte Carlo results obtained using the fixed-order program MCFM 9.1. We also utilized MadGraph5_aMC@NLO, which produced similar results. Our obtained results are computed using the NNPDF30_nlo parton distribution functions with $\alpha_s(M_Z) = 0.118$, interfaced via LHAPDF [55]. The center-of-mass

¹At the transition points between the three regions, we have $\rho/z_{\text{cut}} = R_{\text{sub}}^2$ and R^2 .

energy is set to $\sqrt{s} = 7$ TeV, and jets with transverse momentum $p_t > 150$ GeV and rapidity $|y| < 2.5$ are selected. We set the Z boson decay width to zero to simplify the analysis. The upper plots in figure 1 show the ungroomed distribution for quark (left) and gluon (right) channels, while the lower plots display the trimmed distributions. The jet radius is fixed at $R = 0.7$, with substructure parameters $R_{\text{sub}} = 0.2$ and $z_{\text{cut}} = 0.03$. Renormalization and factorization scales are chosen to be $\mu_R = \mu_F = 150.0$ GeV.

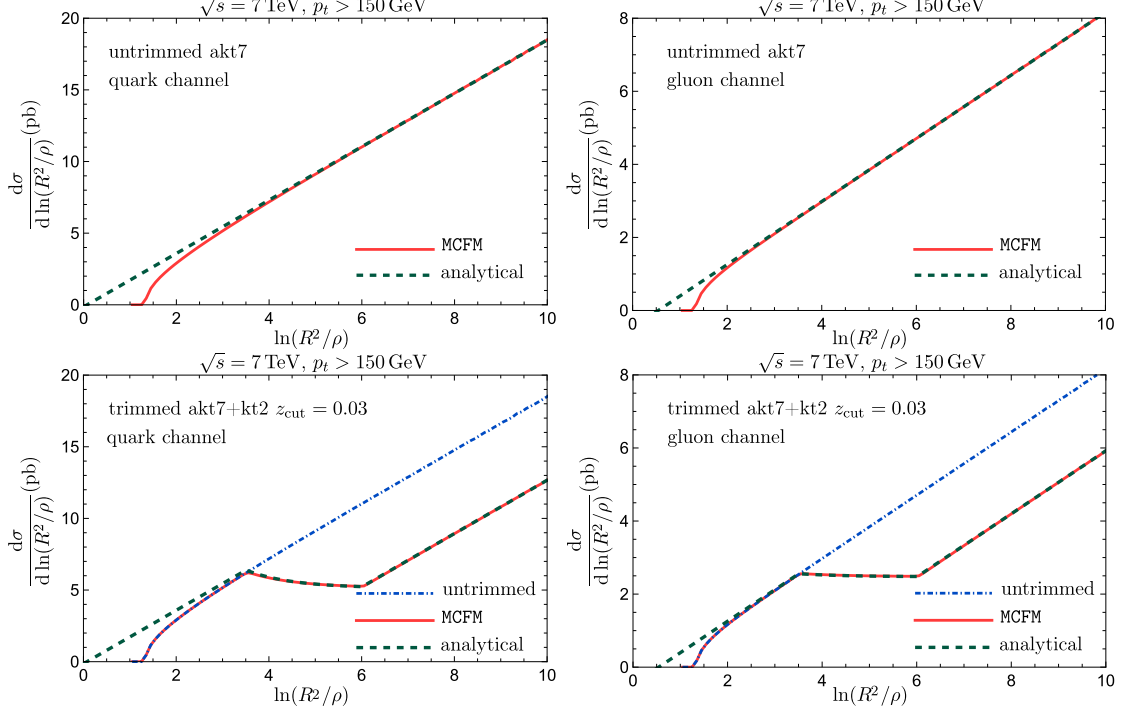


Figure 1. Comparison of the differential jet mass distribution $d\sigma/dL$ between the analytical result and the Monte Carlo result obtained with MCFM, for both untrimmed and trimmed jets. Separate contributions from quark and gluon channels are shown.

In the log-enhanced region, corresponding to small values of ρ , the ungroomed distribution exhibits a linear behavior, confirming the expected structure

$$\frac{d\sigma_\delta}{dL} = \sigma_{0\delta} (g_{11,\delta} + 2g_{12,\delta} L), \quad (3.20)$$

where g_{11} and g_{12} are the coefficients of the single and double logarithms, respectively. In this region, we observe excellent agreement between the Monte Carlo and analytical results, consistent with prior studies [29, 30].

The trimmed distribution also shows strong agreement with the analytical results across the three regions of jet mass. At large ρ (small L), the ungroomed and trimmed distributions converge. In the intermediate region, the trimmed distribution deviates from the double logarithmic behavior in ρ , with the logarithms of ρ being replaced by those in z_{cut} (see

eq. (3.18)). The differential distribution $d\sigma/dL$ remains approximately constant, with any small variations attributable to the ρ -dependence of the jet functions. Finally, in the small- ρ region, the double logarithmic behavior re-emerges with the same coefficient $\sigma_{0\delta} \bar{\alpha}_s C_j/2$ as in the ungroomed case, while the single logarithm (y -intercept) is reduced due to the influence of R_{sub} and z_{cut} dependence.

3.4 NLL' corrections

To achieve NLL' accuracy in the expansion of the cumulative distribution, we must include all terms of the form $\alpha_s^n L^{2n-2}$ at n^{th} order. These terms can be captured by calculating the fixed-order constant $C_1^{(\delta)}$, averaged over the Born configuration \mathcal{B}_δ , as defined in ref. [44]

$$\alpha_s C_1^{(\delta)} \equiv \langle \alpha_s C_1(\mathcal{B}_\delta) \rangle = \frac{1}{\sigma_{0\delta}} \lim_{\rho \rightarrow 0} \left[\int_0^\rho \frac{d\sigma_{\text{NLO}}^{(\delta)}}{d\rho'} d\rho' - \sigma_{\text{NLL},\alpha_s}^{(\delta)}(\rho) \right], \quad (3.21)$$

where $d\sigma_{\text{NLO}}^{(\delta)}/d\rho$ represents the differential distribution obtained from MCFM, and $\sigma_{\text{NLL},\alpha_s}^{(\delta)}(\rho)$ is the NLL-resummed distribution expanded to $\mathcal{O}(\alpha_s)$. The computed values of the constant $\alpha_s C_1^{(\delta)}$, along with the Born and NLO cross-sections, are summarized in table 1.

	$\sigma_{0g}(\text{pb})$	$\sigma_{0q}(\text{pb})$	$\sigma_{1g}(\text{pb})$	$\sigma_{1q}(\text{pb})$	$\alpha_s C_1^{(g)}$	$\alpha_s C_1^{(q)}$
ungroomed	8.23	40.0	14.6	31.8	1.73	0.722
trimmed	8.23	40.0	14.4	31.3	1.71	0.733

Table 1. Numerical results for the Born cross-section, NLO cross-section, and the constant $\alpha_s C_1^{(\delta)}$.

4 Two-loop calculation: NGLs and CLs

4.1 Ungroomed NGLs with anti- k_t and k_t clustering

We begin by reviewing and extending the results for the ungroomed NGLs. At $\mathcal{O}(\alpha_s^2)$, NGLs arise from the correlated emission of two strongly-ordered gluons k_1 and k_2 , where k_1 lies outside the jet and k_2 inside. The non-global contribution at this order is given by [29, 30]

$$f_{\mathcal{B},\delta}^{\text{ungr},(2),\text{NG}}(\rho) = -\frac{1}{2} \bar{\alpha}_s^2 \ln^2 \frac{R^2}{\rho} C_A \sum_{(i\ell)} c_{i\ell} \mathcal{G}_{2,(i\ell)}^{\text{ungr}}(R^2), \quad (4.1a)$$

$$\mathcal{G}_{2,(i\ell)}^{\text{ungr}}(R^2) = \frac{R^4}{4} \int dr_1^2 \frac{d\theta_1}{2\pi} \int dr_2^2 \frac{d\theta_2}{2\pi} \Xi_{\text{NG}}^{\text{ungr}}(k_1, k_2) \mathcal{A}_{i\ell}^{12}, \quad (4.1b)$$

where the two-loop non-Abelian antenna function is defined as

$$\mathcal{A}_{i\ell}^{12} = \omega_{i\ell}^1 (\omega_{i1}^2 + \omega_{1\ell}^2 - \omega_{i\ell}^2). \quad (4.2)$$

The phase-space constraint for anti- k_t clustering is given by ²

$$\Xi_{\text{NG}}^{\text{ungr},\text{akt}}(k_1, k_2) = \Theta(R_{1j}^2 - R^2) \Theta(R^2 - R_{2j}^2), \quad (4.3)$$

²Note that the edge of phase space restricts $R r_i |\sin \theta_i| < \pi$.

while for k_t clustering, it takes the form

$$\Xi_{\text{NG}}^{\text{ungr},k_t}(k_1, k_2) = \Theta(R_{1j}^2 - R^2) \Theta(R^2 - R_{2j}^2) \Theta(R_{12}^2 - R_{2j}^2), \quad (4.4)$$

where the condition $R_{12}^2 > R_{2j}^2$ ensures that gluon k_1 does not pull k_2 out of the jet.

To facilitate the calculation of the NGLs coefficient for the trimmed distribution, we introduce modified phase-space functions

$$\tilde{\Xi}_{\text{NG}}^{\text{akt}}(R^2, R_{\text{sub}}^2) = \Theta(R_{1j}^2 - R^2) \Theta(R_{\text{sub}}^2 - R_{2j}^2), \quad (4.5)$$

$$\begin{aligned} \tilde{\Xi}_{\text{NG}}^{k_t}(R^2, R_{\text{sub}}^2) &= \Theta(R_{1j}^2 - R^2) \Theta(R_{\text{sub}}^2 - R_{2j}^2) \Theta(R_{12}^2 - R_{2j}^2) \\ &= \tilde{\Xi}_{\text{NG}}^{\text{akt}}(R^2, R_{\text{sub}}^2) - \Theta(R_{1j}^2 - R^2) \Theta(R_{\text{sub}}^2 - R_{2j}^2) \Theta(R_{2j}^2 - R_{12}^2), \end{aligned} \quad (4.6)$$

where, for $R_{\text{sub}} < R/2$, the step function $\Theta(R_{2j}^2 - R_{12}^2)$ vanishes, reducing $\tilde{\Xi}_{\text{NG}}^{k_t}(R^2, R_{\text{sub}}^2)$ to $\tilde{\Xi}_{\text{NG}}^{\text{akt}}(R^2, R_{\text{sub}}^2)$. These phase spaces match the anti- k_t and k_t ungroomed cases when $R_{\text{sub}} = R$.

We then define the non-global factor for dipole ($i\ell$) as

$$\mathcal{G}_{2,(i\ell)}(R^2, R_{\text{sub}}^2) = \frac{R^4}{4} \int dr_1^2 \frac{d\theta_1}{2\pi} \int dr_2^2 \frac{d\theta_2}{2\pi} \tilde{\Xi}_{\text{NG}}(R^2, R_{\text{sub}}^2) \mathcal{A}_{i\ell}^{12}, \quad (4.7)$$

such that $\mathcal{G}_{2,(i\ell)}^{\text{ungr},\text{akt}}(R^2) = \mathcal{G}_{2,(i\ell)}^{\text{akt}}(R^2, R^2)$ and $\mathcal{G}_{2,(i\ell)}^{\text{ungr},k_t}(R^2) = \mathcal{G}_{2,(i\ell)}^{k_t}(R^2, R^2)$. Expanding the integrand as a power series in R and performing the relevant integrations we obtain the following results

$$\begin{aligned} \mathcal{G}_{2,(ab)}^{\text{akt}}(R^2, R_{\text{sub}}^2) &= -\frac{1}{2} R^2 \ln R^2 + (\mathcal{J}_{ab}(R^2) - \mathcal{J}_{ab}(R_{\text{sub}}^2)) \ln(R^2 - R_{\text{sub}}^2) \\ &\quad + \frac{1}{2} R_{\text{sub}}^2 + \frac{1}{8} R^2 R_{\text{sub}}^2 - \frac{1}{576} R^4 R_{\text{sub}}^2 - \frac{1}{576} R^2 R_{\text{sub}}^4 + \mathcal{O}(R^8), \end{aligned} \quad (4.8a)$$

$$\begin{aligned} \mathcal{G}_{2,(aj)}^{\text{akt}}(R^2, R_{\text{sub}}^2) &= \mathcal{G}_{2,(bj)}^{\text{akt}}(R^2, R_{\text{sub}}^2) = (\mathcal{J}_{aj}(R^2) - \mathcal{J}_{aj}(R_{\text{sub}}^2)) \ln \frac{R^2 - R_{\text{sub}}^2}{R^2} \\ &\quad + \frac{1}{2} \text{Li}_2 \frac{R_{\text{sub}}^2}{R^2} + \frac{5}{576} R^2 R_{\text{sub}}^2 - \frac{1}{192} R_{\text{sub}}^4 + \mathcal{O}(R^8). \end{aligned} \quad (4.8b)$$

for anti- k_t clustering, and

$$\begin{aligned} \mathcal{G}_{2,(ab)}^{k_t}(R^2, R_{\text{sub}}^2) &= \mathcal{G}_{2,(ab)}^{\text{akt}}(R^2, R_{\text{sub}}^2) \\ &\quad - \Theta(2R_{\text{sub}} - R) [\chi_2(x) R^2 + \chi_4(x) R^4 + \chi_6(x) R^6 + \mathcal{O}(R^8)], \end{aligned} \quad (4.9a)$$

$$\begin{aligned} \mathcal{G}_{2,(aj)}^{k_t}(R^2, R_{\text{sub}}^2) &= \mathcal{G}_{2,(bj)}^{k_t}(R^2, R_{\text{sub}}^2) = \mathcal{G}_{2,(aj)}^{\text{akt}}(R^2, R_{\text{sub}}^2) \\ &\quad - \Theta(2R_{\text{sub}} - R) [\psi_0(x) + \psi_2(x) R^2 + \psi_4(x) R^4 + \psi_6(x) R^6 + \mathcal{O}(R^8)], \end{aligned} \quad (4.9b)$$

for k_t clustering, where the higher-order terms, $\mathcal{O}(R^8)$, are negligibly small.

The coefficient functions $\chi_i(x)$ (for the dipole (ab)) and $\psi_i(x)$ (for the dipoles (aj) and (bj)), which appear in the k_t clustering non-global factors, depend on the ratio $x = R_{\text{sub}}/R$, with $x > 1/2$. These coefficients have been evaluated numerically and are presented in Table 2 for selected values of x .

x	χ_2	χ_4	χ_6	ψ_0	ψ_2	ψ_4	ψ_6
0.5	0.0000	0.0000	0.0000	0.0000	0.0000	0.000	0.000
0.6	0.0047	-0.0003	2.3×10^{-6}	0.0076	0.0011	-2.1×10^{-5}	-1.3×10^{-6}
0.7	0.0288	-0.0019	1.6×10^{-5}	0.0394	0.0062	-0.00012	-9.4×10^{-6}
0.8	0.0881	-0.0060	5.5×10^{-5}	0.1040	0.0183	-0.00035	-3.3×10^{-5}
0.9	0.2080	-0.0135	0.00014	0.2167	0.0430	-0.00063	-8.8×10^{-5}
1.0	0.4846	-0.0258	0.00031	0.4569	0.1034	-0.00038	-0.00019

Table 2. The numerically computed coefficients of the series in eq. (4.9) for the k_t clustering non-global factors, evaluated for selected values of $x = R_{\text{sub}}/R$. For $x \leq 1/2$, these coefficients vanish.

The results for the non-global factors $\mathcal{G}_{2,(i\ell)}(R^2, R_{\text{sub}}^2)$ have been validated through numerical integration and provide a good approximation even for R of order unity. When $R_{\text{sub}} = R$, the results are consistent with those found in refs. [29, 30] for the non-global coefficients in the ungroomed distribution

$$\mathcal{G}_{2,(ab)}^{\text{akt}}(R^2, R^2) = -\frac{1}{2} R^2 \ln R^2 + \frac{1}{2} R^2 + \frac{1}{8} R^4 - \frac{1}{288} R^6 + \mathcal{O}(R^8), \quad (4.10a)$$

$$\mathcal{G}_{2,(aj)}^{\text{akt}}(R^2, R^2) = \mathcal{G}_{2,(bj)}(R^2, R^2) = \frac{\pi^2}{12} + \frac{1}{288} R^4 + \mathcal{O}(R^8). \quad (4.10b)$$

$$\mathcal{G}_{2,(ab)}^{\text{kt}}(R^2, R^2) = \mathcal{G}_{2,(ab)}^{\text{akt}}(R^2) - 0.4846 R^2 + 0.0258 R^4 - 0.0003 R^6 + \mathcal{O}(R^8), \quad (4.10c)$$

$$\mathcal{G}_{2,(aj)}^{\text{kt}}(R^2, R^2) = \mathcal{G}_{2,(aj)}^{\text{akt}}(R^2) - 0.4569 - 0.1034 R^2 + 0.0004 R^4 + 0.0002 R^6 + \mathcal{O}(R^8). \quad (4.10d)$$

4.2 Trimmed NGLs

Now we calculate the non-global contribution to the trimmed jet mass distribution at two loops. The jet is defined by applying anti- k_t clustering to the final states, followed by the trimming procedure using k_t clustering for the sub-jets.

NGLs arise from a mis-cancellation between real and virtual contributions when the secondary soft emission k_2 remains within the groomed jet, while the harder emission k_1 is outside the jet. This scenario can occur in two ways: (1) gluon k_1 is outside the jet from the beginning, while gluon k_2 remains inside and untrimmed, or (2) both gluons k_1 and k_2 are initially inside the jet, but k_1 is trimmed away while k_2 remains untrimmed. In the latter case, gluon k_2 must be k_t -clustered into the jet at the substructure stage, implying $R_{\text{sub}}^2 > R_{2j}^2$ and $R_{12}^2 > R_{2j}^2$.

The corresponding angular phase space is given by the expression

$$\begin{aligned} \Xi_{\text{NG}}^{\text{trim}}(k_1, k_2) = & \Theta(R_{1j}^2 - R^2) \Theta(R_{\text{sub}}^2 - R_{2j}^2) \\ & + \Theta(R_{1j}^2 - R^2) \Theta(R^2 - R_{2j}^2) \Theta(R_{2j}^2 - R_{\text{sub}}^2) \Theta(\xi_2 - z_{\text{cut}}) \\ & + \Theta(R^2 - R_{1j}^2) \Theta(R_{1j}^2 - R_{\text{sub}}^2) \Theta(z_{\text{cut}} - \xi_1) \Theta(R_{\text{sub}}^2 - R_{2j}^2) \Theta(R_{12}^2 - R_{2j}^2). \end{aligned} \quad (4.11)$$

This phase space is further constrained by the following cuts on gluon energies

$$\Phi(\xi_1, \xi_2) = \Theta(\xi_1 - \xi_2) \Theta(\xi_2 R_{2j}^2 - \rho). \quad (4.12)$$

The phase space can be simplified in terms of the ρ variable regions, found at one loop, as follows

- Large- ρ region, $\rho > R^2 z_{\text{cut}}$

$$\Phi(\xi_1, \xi_2) \Xi_{\text{NG}}^{\text{trim}}(k_1, k_2) = \Phi(\xi_1, \xi_2) \Theta(R_{1j}^2 - R^2) \Theta(R^2 - R_{2j}^2). \quad (4.13)$$

- Intermediate- ρ region, $R_{\text{sub}}^2 z_{\text{cut}} < \rho < R^2 z_{\text{cut}}$

$$\begin{aligned} \Phi(\xi_1, \xi_2) \Xi_{\text{NG}}^{\text{trim}} &= [\Phi(\xi_1, \xi_2) - \Theta(\xi_1 - \xi_2) \Theta(\xi_2 - z_{\text{cut}})] \Theta(R_{1j}^2 - R^2) \Theta(\rho/z_{\text{cut}} - R_{2j}^2) \\ &\quad + \Theta(\xi_1 - \xi_2) \Theta(\xi_2 - z_{\text{cut}}) \Theta(R_{1j}^2 - R^2) \Theta(R^2 - R_{2j}^2). \end{aligned} \quad (4.14)$$

- Small- ρ region, $\rho < R_{\text{sub}}^2 z_{\text{cut}}$

$$\begin{aligned} \Phi(\xi_1, \xi_2) \Xi_{\text{NG}}^{\text{trim}} &= [\Phi(\xi_1, \xi_2) - \Theta(\xi_1 - \xi_2) \Theta(\xi_2 - z_{\text{cut}})] \Theta(R_{1j}^2 - R^2) \Theta(R_{\text{sub}}^2 - R_{2j}^2) \\ &\quad + \Theta(\xi_1 - \xi_2) \Theta(\xi_2 - z_{\text{cut}}) \Theta(R_{1j}^2 - R^2) \Theta(R^2 - R_{2j}^2) \\ &\quad + \Phi(\xi_1, \xi_2) \Theta(z_{\text{cut}} - \xi_1) \Theta(R^2 - R_{1j}^2) \Theta(R_{1j}^2 - R_{\text{sub}}^2) \\ &\quad \times \Theta(R_{\text{sub}}^2 - R_{2j}^2) \Theta(R_{12}^2 - R_{2j}^2) \Theta(R_{2j}^2 - \rho/z_{\text{cut}}). \end{aligned} \quad (4.15)$$

In the large- ρ region, the phase space is identical to that which generates the NGLs for the ungroomed jet mass distribution, $\tilde{\Xi}_{\text{NG}}^{\text{akt}}(R^2, R^2)$. Therefore, trimming has no effect in this region, similar to the one-loop case.

At this order, the result can be expressed as

$$\begin{aligned} f_{\mathcal{B}, \delta}^{\text{trim}, (2), \text{NG}}(\rho) &= -\frac{1}{2} \bar{\alpha}_s^2 C_A \sum_{(i\ell)} \mathcal{C}_{i\ell} \left(\ln^2 \min \left[\frac{R^2}{\rho}, \frac{1}{z_{\text{cut}}} \right] \mathcal{G}_{2, (i\ell)}^{\text{akt}}(R^2, R^2) \right. \\ &\quad + \Theta(R^2 z_{\text{cut}} - \rho) \left[\ln^2 \frac{R^2}{\rho} - \ln^2 \frac{1}{z_{\text{cut}}} \right] \mathcal{G}_{2, (i\ell)}^{\text{akt}}(R^2, \max[\rho/z_{\text{cut}}, R_{\text{sub}}^2]) \\ &\quad + \Theta(R_{\text{sub}}^2 z_{\text{cut}} - \rho) \ln^2 \frac{R_{\text{sub}}^2 z_{\text{cut}}}{\rho} \left[\mathcal{G}_{2, (i\ell)}^{\text{kt}}(R_{\text{sub}}^2, R_{\text{sub}}^2) - \mathcal{G}_{2, (i\ell)}^{\text{kt}}(R_{\text{sub}}^2, \rho/z_{\text{cut}}) \right. \\ &\quad \left. \left. + \mathcal{G}_{2, (i\ell)}^{\text{kt}}(R^2, \rho/z_{\text{cut}}) - \mathcal{G}_{2, (i\ell)}^{\text{kt}}(R^2, R_{\text{sub}}^2) \right] \right). \end{aligned} \quad (4.16)$$

4.3 Ungroomed CLs with k_t clustering

We recall that the ungroomed CLs emerge specifically when the k_t clustering algorithm is applied to the final states rather than the anti- k_t algorithm. At the two loop level, these logarithms arise when two strongly-ordered gluons are emitted directly from the hard partons. In this scenario, the harder gluon k_1 lies outside the jet while the softer gluon k_2 is initially inside. However, k_2 is closer to k_1 than to the jet-initiating parton, leading to k_2 being pulled out by k_1 and consequently leaving the jet massless. In the virtual corrections, when k_1 is virtual, the gluon k_2 remains inside the jet resulting in a non-zero jet mass. The mismatch between real and virtual contributions gives the clustering logarithmic term

$$f_{\mathcal{B}, \delta}^{\text{ungr}, (2), \text{CL}}(\rho) = \frac{1}{2} \bar{\alpha}_s^2 \ln^2 \frac{R^2}{\rho} \sum_{(ik, \ell m)} \mathcal{C}_{ik} \mathcal{C}_{\ell m} \mathcal{F}_{2, (ik, \ell m)}^{\text{ungr}}(R^2), \quad (4.17)$$

$$\mathcal{F}_{2, (ik, \ell m)}^{\text{ungr}}(R^2) = \frac{R^4}{4} \int dr_1^2 \frac{d\theta_1}{2\pi} \int dr_2^2 \frac{d\theta_2}{2\pi} \Xi_{\text{CL}}^{\text{ungr}}(k_1, k_2) \omega_{ik}^1 \omega_{\ell m}^2, \quad (4.18)$$

where the ungroomed phase space is defined as

$$\Xi_{\text{CL}}^{\text{ungr}}(k_1, k_2) = \Theta(R_{1j}^2 - R^2) \Theta(R^2 - R_{2j}^2) \Theta(R_{2j}^2 - R_{12}^2). \quad (4.19)$$

To introduce the trimmed CLs more effectively, we define the modified phase space

$$\tilde{\Xi}_{\text{CL}}(R^2, R_{\text{sub}}^2) = \Theta(R_{1j}^2 - R^2) \Theta(R_{\text{sub}}^2 - R_{2j}^2) \Theta(R_{2j}^2 - R_{12}^2), \quad (4.20)$$

such that $\Xi_{\text{CL}}^{\text{ungr}}(k_1, k_2) = \tilde{\Xi}_{\text{CL}}(R^2, R^2)$. We define the clustering factor for dipole pairs $(ik, \ell m)$ as

$$\mathcal{F}_{2,(ik,\ell m)}(R^2, R_{\text{sub}}^2) = \frac{R^4}{4} \int dr_1^2 \frac{d\theta_1}{2\pi} \int dr_2^2 \frac{d\theta_2}{2\pi} \tilde{\Xi}_{\text{CL}}(R^2, R_{\text{sub}}^2) \omega_{ik}^1 \omega_{\ell m}^2. \quad (4.21)$$

Similar to the non-global factor for k_t clustering, these coefficients vanish when the fraction $x = R_{\text{sub}}/R$ is less than $1/2$. The clustering factors can be expanded as a series in the radius parameter R , with coefficients dependent on x as follows

$$\mathcal{F}_{2,(ab,ab)} = \gamma(x) R^4, \quad (4.22a)$$

$$\mathcal{F}_{2,(ab,aj)} = \mathcal{F}_{2,(ab,bj)} = \mu_2(x) R^2 + \mu_4(x) R^4 + \mu_6(x) R^6 + \mathcal{O}(R^8), \quad (4.22b)$$

$$\mathcal{F}_{2,(aj,ab)} = \mathcal{F}_{2,(bj,ab)} = \sigma_2(x) R^2 + \sigma_4(x) R^4 + \sigma_6(x) R^6 + \mathcal{O}(R^8), \quad (4.22c)$$

$$\mathcal{F}_{2,(aj,aj)} = \mathcal{F}_{2,(bj,bj)} = \tau_0(x) + \tau_2(x) R^2 + \tau_4(x) R^4 + \tau_6(x) R^6 + \mathcal{O}(R^8), \quad (4.22d)$$

$$\mathcal{F}_{2,(aj,bj)} = \mathcal{F}_{2,(bj,aj)} = \nu_0(x) + \nu_2(x) R^2 + \nu_4(x) R^4 + \nu_6(x) R^6 + \mathcal{O}(R^8). \quad (4.22e)$$

The coefficient functions $\gamma(x)$, $\mu_i(x)$, $\sigma_i(x)$, $\tau_i(x)$, and $\nu_i(x)$, are evaluated analytically when possible, otherwise numerically, as detailed in Appendix B. For $R_{\text{sub}} = R$, these CL coefficients agree with those found in ref. [30]

$$\mathcal{F}_{2,(ab,ab)}(R^2, R^2) = 0.0517 R^4, \quad (4.23a)$$

$$\mathcal{F}_{2,(ab,aj)} = \mathcal{F}_{2,(ab,bj)} = 0.0715 R^2 + 0.0129 R^4 + 0.0003 R^6 + \mathcal{O}(R^8), \quad (4.23b)$$

$$\mathcal{F}_{2,(aj,ab)} = \mathcal{F}_{2,(bj,ab)} = 0.0319 R^2 + 0.0129 R^4 + 0.0006 R^6 + \mathcal{O}(R^8), \quad (4.23c)$$

$$\mathcal{F}_{2,(aj,aj)} = \mathcal{F}_{2,(bj,bj)} = 0.0457 + 0.0475 R^2 + 0.0091 R^4 + 0.0004 R^6 + \mathcal{O}(R^8), \quad (4.23d)$$

$$\mathcal{F}_{2,(aj,bj)} = \mathcal{F}_{2,(bj,aj)} = 0.0457 + 0.0042 R^2 + 0.0004 R^4 + 0.00004 R^6 + \mathcal{O}(R^8). \quad (4.23e)$$

4.4 Trimmed CLs

When grooming is applied, using the anti- k_t algorithm for both seed-jet finding and sub-jet substructure eliminates CLs contributions. However, as considered in this paper, employing anti- k_t for jet finding followed by k_t clustering for sub-jet substructure introduces a CLs contribution. The phase space in this case is given by

$$\Xi_{\text{CL}}^{\text{trim}}(k_1, k_2) = \Theta(R^2 - R_{1j}^2) \Theta(R_{1j}^2 - R_{\text{sub}}^2) \Theta(R_{\text{sub}}^2 - R_{2j}^2) \Theta(R_{2j}^2 - R_{12}^2) \Theta(z_{\text{cut}} - \xi_1). \quad (4.24)$$

This phase space is further constrained by the cuts $\Phi(\xi_1, \xi_2) = \Theta(\xi_1 - \xi_2) \Theta(\xi_2 R_{2j}^2 - \rho)$, analogous to the non-global case.

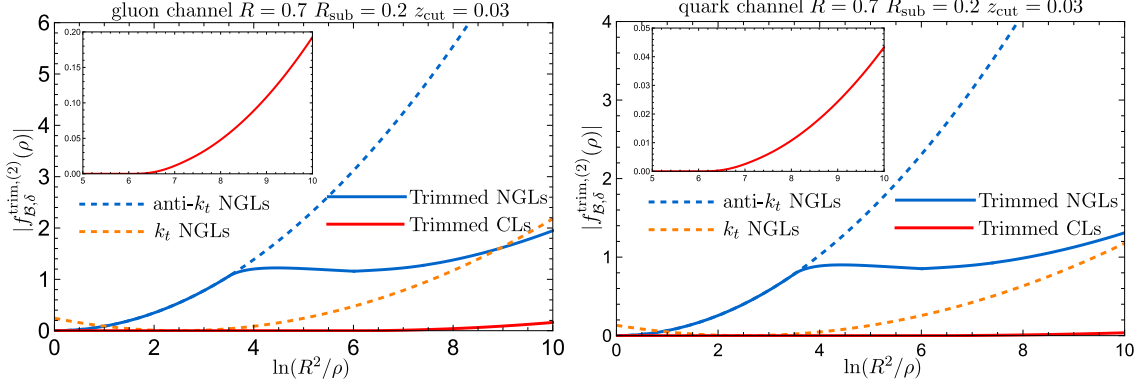


Figure 2. NGLs and CLs contributions to the jet mass distribution at second order. The NGLs contribution is negative while the CLs is positive. The absolute values of the results are shown for comparison.

In this setup, k_1 lies within the annular region $R_{\text{sub}} < R_{1j} < R$, while k_2 is located in the hard sub-jet region, $R_{2j} < R_{\text{sub}}$. Both gluons k_1 and k_2 are initially clustered to the seed jet via anti- k_t . During the substructure phase, k_t clustering is applied to the seed-jet constituents. If $R_{2j} < R_{12}$, k_2 evades clustering with the hard jet and instead clusters with k_1 . The sub-jet formed by k_1 and k_2 is then rejected if $k_{t1} < z_{\text{cut}} p_t$. On the other hand, if k_1 is virtual, k_2 remains within the hard sub-jet, leading to a non-zero jet mass.

The phase space can then be expressed as

$$\begin{aligned} \Phi(\xi_1, \xi_2) \Xi_{\text{CL}}^{\text{trim}} &= \Phi(\xi_1, \xi_2) \Theta(z_{\text{cut}} - \xi_1) \Theta(R_{1j}^2 - R_{\text{sub}}^2) \\ &\times \Theta(R_{\text{sub}}^2 - R_{2j}^2) \Theta(R_{2j}^2 - R_{12}^2) \Theta(R_{2j}^2 - \rho/z_{\text{cut}}), \end{aligned} \quad (4.25)$$

assuming $R_{\text{sub}} < R/2$. This assumption implies that $\Theta(R^2 - R_{1j}^2) = 1$, making the phase space independent of R . Consequently, CLs only appear in the small- ρ region, where $\rho < z_{\text{cut}} R_{\text{sub}}^2$. Therefore, the result is written as

$$\begin{aligned} f_{\mathcal{B},\delta}^{\text{trim,(2),CL}}(\rho) &= \Theta(R_{\text{sub}}^2 z_{\text{cut}} - \rho) \frac{1}{2} \bar{\alpha}_s^2 \ln^2 \frac{R_{\text{sub}}^2 z_{\text{cut}}}{\rho} \sum_{(ik,\ell m)} \mathcal{C}_{ik} \mathcal{C}_{\ell m} [\mathcal{F}_{2,(ik,\ell m)}(R_{\text{sub}}^2, R_{\text{sub}}^2) \\ &\quad - \Theta\left(\rho - \frac{1}{4} R_{\text{sub}}^2 z_{\text{cut}}\right) \mathcal{F}_{2,(ik,\ell m)}(R_{\text{sub}}^2, \rho/z_{\text{cut}})] . \end{aligned} \quad (4.26)$$

In the figure 2, we present the clustering and non-global contributions, $f_{\mathcal{B},\delta}^{\text{trim,(2),NG}}(\rho)$ and $f_{\mathcal{B},\delta}^{\text{trim,(2),CL}}(\rho)$, for both channels δ . Additionally, we show the NGLs contribution for anti- k_t jets with $R = 0.7$.

We observe that the NGLs contribution is significantly larger with anti- k_t clustering compared to k_t clustering. When applying the trimming algorithm, the NGLs in the large- ρ region coincide with those of anti- k_t clustering but start to deviate in the intermediate and small- ρ regions. In these smaller- ρ regions, the NGLs become comparable in size to those observed with k_t clustering as ρ decreases. On the other hand, the CLs contribution is confined to the small- ρ region and is much smaller compared to the NGLs.

In the next subsection, we will perform the resummation of NGLs to all orders.

4.5 NGLs at all orders

Let us begin by briefly reviewing the resummation of NGLs and CLs to all orders using the k_t and anti- k_t clustering algorithms within the large- N_c approximation. This resummation is carried out numerically via the Monte Carlo dipole-evolution program described in refs. [32, 33].

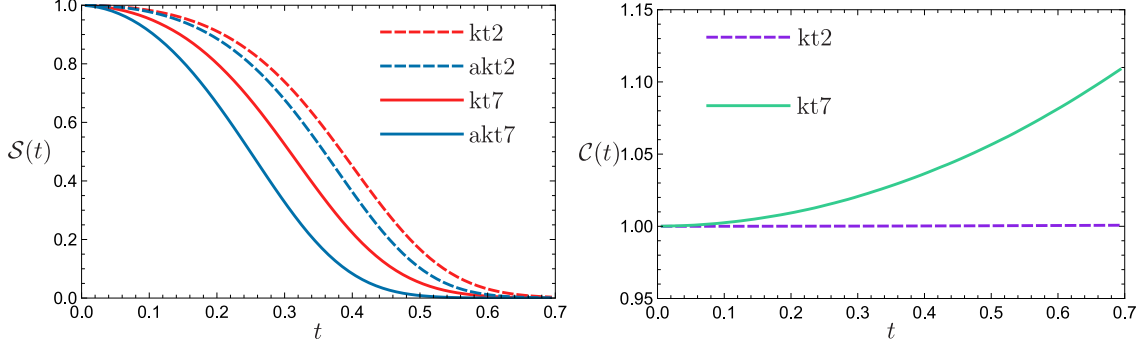


Figure 3. Resummed NGLs and CLs factors $\mathcal{S}(t)$ and $\mathcal{C}(t)$ for ungroomed k_t and anti- k_t clustered jets. Results for dipole (ab) are displayed.

Figure 3 presents the resummed NGLs factor $\mathcal{S}(t)$ for dipole (ab) using both clustering algorithms with jet radii $R = 0.7$ and $R = 0.2$, alongside the resummed CLs factor $\mathcal{C}(t)$ for k_t clustering, all plotted as a function of the evolution parameter t . The evolution parameter t is defined as

$$t(L) = -\frac{1}{4\pi\beta_0} \ln(1 - 2\alpha_s\beta_0 L), \quad (4.27)$$

where at leading order, $t \rightarrow \frac{1}{2} \bar{\alpha}_s L$.

One notable observation is that NGLs are reduced when using k_t clustering (with the form factor closer to unity), and they become even smaller for a jet radius of $R = 0.2$. As discussed in the previous subsection, CLs are negligible for $R = 0.2$, with the form factor $\mathcal{C} \sim 1$ for this radius. For instance, at $t = 0.7$ (corresponding to $L \sim 6.78$), the two-loop contributions $f_{\mathcal{B},q}^{\text{trim},(2),\text{CL}}(\rho) \sim 0.0066$ and $f_{\mathcal{B},g}^{\text{trim},(2),\text{CL}}(\rho) \sim 0.0015$ are numerically insignificant.

For the trimmed distribution, we perform the resummation of NGLs to all orders incorporating the trimming effect in the Monte Carlo program of ref. [32, 33]. Figure 4 displays the resummed factor $\mathcal{S}(t)$ for different configurations: $R = 0.7$ anti- k_t clustering (akt7), $R = 0.2$ k_t clustering (kt2), and $R = 0.7$ with $R_{\text{sub}} = 0.2$ for the trimmed distribution (trmd72).

In this plot, the trmd72 distribution overlaps with the akt7 distribution at small t (corresponding to large ρ). However, for $t > t_{\text{cut}} = t(L_{\text{cut}})$, with $L_{\text{cut}} = \ln(1/z_{\text{cut}})$, the trmd72 distribution departs from the akt7 distribution and eventually approaches the kt2 distribution at large t values.

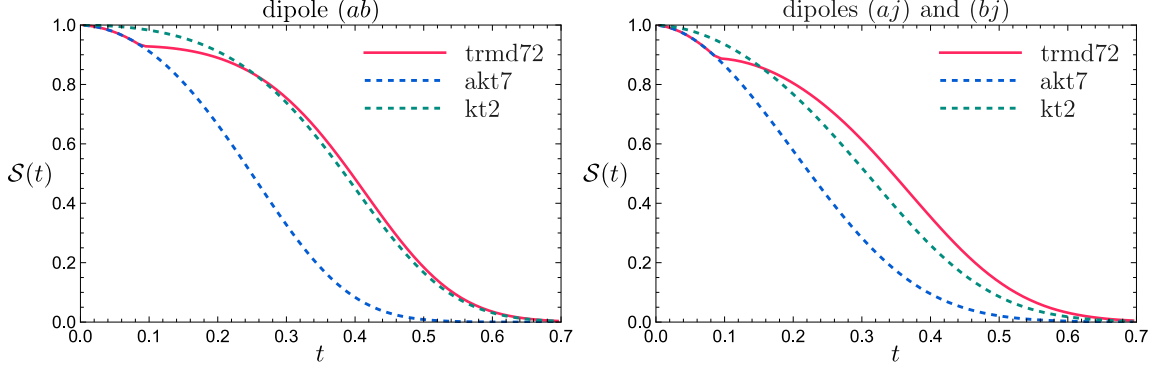


Figure 4. Resummed NGLs factor $\mathcal{S}(t)$ for trimmed jets. Results for dipole (ab) are displayed on the left, and those for dipoles (aj) and (bj) are shown on the right.

n	2	3	4	5
$\mathcal{I}_{(ab)}^{(n)}$	0.449	0.153	0.048	1.242
$\mathcal{I}_{(aj)}^{(n)}$ and $\mathcal{I}_{(bj)}^{(n)}$	0.823	-0.337	0.380	0.429
$\tilde{\mathcal{I}}_{(ab)}^{(n)}$	NA	-0.624	3.575	-4.989
$\tilde{\mathcal{I}}_{(aj)}^{(n)}$ and $\tilde{\mathcal{I}}_{(bj)}^{(n)}$	NA	-1.214	7.795	-12.282

Table 3. The fitting parameters for the Monte Carlo data for the resummed NGLs.

To incorporate the NGLs into the anti- k_t ungroomed distribution, we parameterize the form factor for each dipole $(i\ell)$ as follows

$$\mathcal{S}_{(i\ell)}(t) = \exp \left(-\frac{\mathcal{C}_{i\ell}}{\mathcal{C}_A} \sum_{n=2}^{\infty} \mathcal{I}_{i\ell}^{(n)} \frac{(2 \mathcal{C}_A t)^n}{n!} \right), \quad (4.28)$$

where the leading-order term is calculated at $\mathcal{O}(\alpha_s^2)$, i.e., $\mathcal{I}_{i\ell}^{(2)} = \mathcal{G}_{2,(i\ell)}(R^2, R^2)$. Numerically we have $\mathcal{I}_{ab}^{(2)} = 0.449$ and $\mathcal{I}_{aj}^{(2)} = \mathcal{I}_{bj}^{(2)} = 0.823$. The color factor used in the fit is $\mathcal{C}_{i\ell} = 2 \mathcal{C}_F$ since the dipole-evolution code assumes a $q\bar{q}$ dipole. In the large- N_c limit, this factor is set to $2 \mathcal{C}_F \rightarrow \mathcal{C}_A$, but for phenomenology, we restore the actual color factors.

The polynomial series in the exponent is truncated once it provides a reasonable fit to the Monte Carlo data. Truncating at $n = 5$ offers an accurate description of the Monte Carlo results, with errors at the percent level. The obtained fitting parameters are shown in table 3.

The obtained coefficients $\mathcal{I}^{(n)}$ are then used in the full non-global form factor, which for the ungroomed distribution is expressed for each channel as

$$\mathcal{S}_{\delta}^{\text{ungr}}(t) = \exp \left(-\sum_{(i\ell)} \frac{\mathcal{C}_{i\ell}}{\mathcal{C}_A} \sum_{n=2}^{\infty} \mathcal{I}_{i\ell}^{(n)} \frac{(2 \mathcal{C}_A t)^n}{n!} \right). \quad (4.29)$$

The trimmed non-global factor can similarly be fitted using the following expression

$$\mathcal{S}_{(i\ell)}^{\text{trim}}(t, t_{\text{cut}}, t_{\text{sub}}) = \exp \left(f_{\mathcal{B},(i\ell)}^{\text{trim},(2),\text{NG}}(t, t_{\text{cut}}, t_{\text{sub}}) - \frac{\mathcal{C}_{i\ell}}{C_A} \sum_{n=3} \mathcal{I}_{i\ell}^{(n)} \frac{(2 C_A \min[t, t_{\text{cut}}])^n}{n!} \right. \\ \left. - \Theta(t - t_{\text{cut}}) \frac{\mathcal{C}_{i\ell}}{C_A} \sum_{n=3} \tilde{\mathcal{I}}_{i\ell}^{(n)} \frac{(2 C_A)^n}{n!} (t^n - t_{\text{cut}}^n) \right). \quad (4.30)$$

Here, $f_{\mathcal{B},(i\ell)}^{\text{trim},(2),\text{NG}}(t, t_{\text{cut}}, t_{\text{sub}})$ is obtained by replacing $\bar{\alpha}_s \ln(R^2/\rho)$ with $2t$, $\bar{\alpha}_s \ln(1/z_{\text{cut}})$ with $2t_{\text{cut}}$, and $\bar{\alpha}_s \ln(R_{\text{sub}}^2/\rho)$ with $2t_{\text{sub}}$ in the expression (4.16). This form ensures that the expansion of this resummed factor reproduces the $\mathcal{O}(\alpha_s^2)$ results for NGLs obtained in the previous subsection. The obtained coefficients $\tilde{\mathcal{I}}_{i\ell}^{(n)}$ are listed in table 3.

Since the CLs have a numerically insignificant impact, we neglect their all-orders resummation.

5 Convolution and numerical results

In this section, we present the numerical results for the convolution of the resummed form factor, including resummed NGLs at large N_c , with the Born cross-section. We use the Monte Carlo program `MadGraph5_aMC@NLO` [45, 46] to generate Born-level events for the process $pp \rightarrow Z + \text{jet}$ at parton level. The generated events are subject to selection cuts $\Omega_{\mathcal{B}}$, specifically requiring the jet to have $p_t > 150$ GeV and $|y| < 2.5$. We employ `NNPDF30_nlo` parton distribution functions with factorization and renormalization scales set to 150 GeV.

The resulting LHE event sample is accessed with `MadAnalysis 5` analysis package [56] to extract the flavor and kinematics of the hard partons in each event. For each bin of the ρ variable, events are weighted with the resummed form factor, and the weights are summed over all events. The integrated distribution, as given in eq. (2.6), is then obtained by dividing the summed weights by the effective luminosity, $\mathcal{L} = N_{\text{tot}}/\sigma_0$, where N_{tot} is the total number of generated events, and σ_0 is the Born cross-section obtained from `MadGraph5_aMC@NLO` event generator. The differential distribution is calculated through numerical differentiation of the integrated distribution.

To illustrate the impact of NGLs and the constant $\alpha_s C_1$, we plot three configurations of the resummed distribution in figure 5: (a) resumming global logarithms only, (b) resumming both global and non-global logarithms, and (c) the full resummed distribution, valid at NLL' accuracy, including the constant C_1 . The plots show differential distributions in $\sqrt{\rho}$ normalized to the Born cross-section for the global and resummed distributions, and normalized to the NLO cross-section for the distribution accounting for the constant C_1 . Results are shown for both ungroomed and trimmed jets.

Our results highlight the significant impact of the non-global contributions on the ungroomed distribution, particularly in the region where large logarithms are dominant. While the non-global effects are less pronounced for the trimmed distribution, they remain non-negligible.

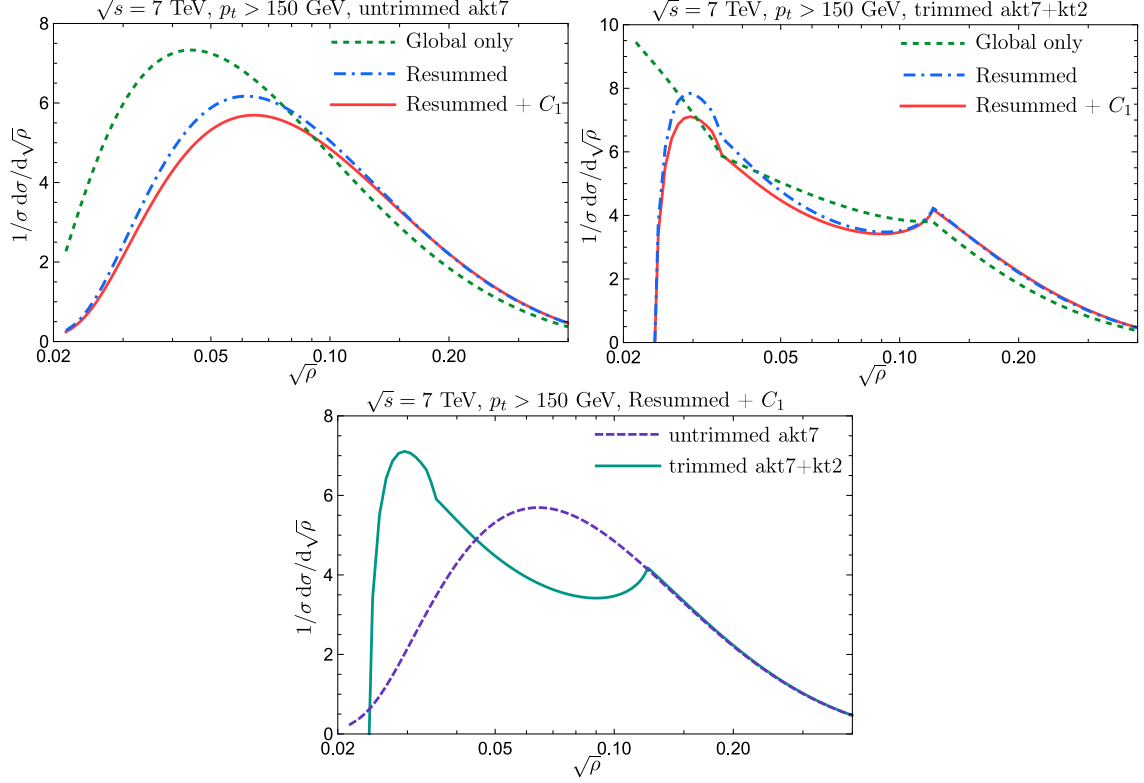


Figure 5. Resummed differential distributions of the jet mass observable, comparing trimmed and untrimmed cases. The plots display results for global logarithms, global and non-global logarithms, and the full resummation at NLL' accuracy.

It is important to note that due to the Landau pole singularity, the distribution becomes unreliable for ρ values to the left of the peak, roughly corresponding to $\sqrt{\rho}$ less than 0.03. This region is also heavily influenced by non-perturbative effects, which are not accounted for in these plots. Additionally, matching to fixed-order NLO results is necessary to correct the behavior of the distribution at the tail, making it comparable to experimental data. We leave these tasks to our future work.

The peak of the untrimmed distribution is more distinct and occurs at a higher mass value than that of the trimmed distribution. This behavior is consistent with the removal of soft and wide-angle radiation from the jet in the trimming process, resulting in a lower overall mass. This trend aligns with the observations from parton shower simulations, as shown in figure 6.

Figure 6 compares our resummed results, valid at NLL accuracy in the exponent and NLL' accuracy in the expansion, to parton-level Monte Carlo simulations from Pythia 8.3 [47, 48], Herwig++ [49, 50], and Sherpa 2.2 [51]. The Pythia 8 and Herwig++ results are obtained by showering NLO events from MadGraph5_aMC@NLO. Jet finding for both un-groomed and groomed jets is performed using FastJet [57] and its plugin FastJet-Contrib.

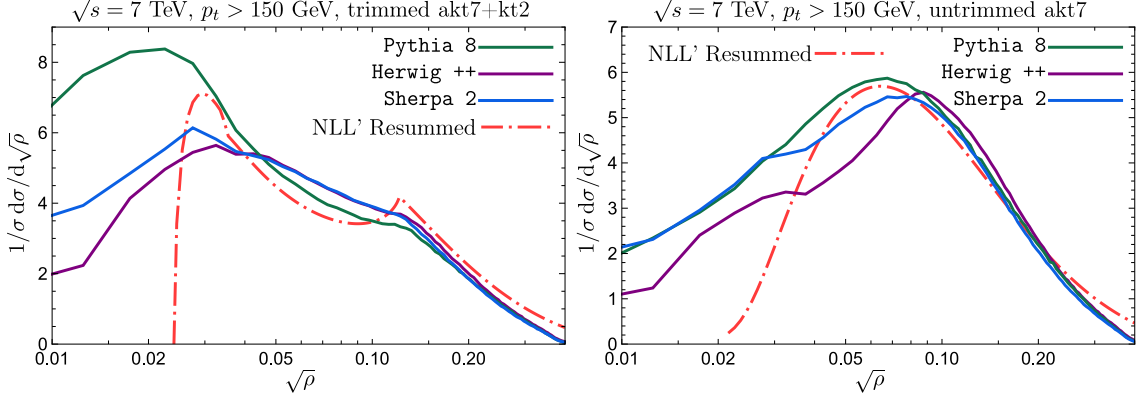


Figure 6. Comparison of trimmed (left) and untrimmed (right) resummed jet mass distributions with Monte Carlo simulations from parton showers: Pythia 8.3, Herwig++, and Sherpa 2.2.

We observe good agreement between our results and the Pythia 8 parton shower, particularly away from the region affected by the Landau pole singularity. For the ungroomed distribution, Sherpa and Herwig++ show a distorted peak, particularly to the left of it. As observed in our previous work [30], this distortion and the discrepancies between different Monte Carlo simulations diminish once non-perturbative effects are included. A similar observation is made for the trimmed distribution, where significant differences between Pythia 8 and Herwig++/Sherpa are observed for $\sqrt{\rho}$ values less than 0.05.

6 Conclusions

In this paper we have presented a detailed calculation of the resummed trimmed jet mass distribution at NLL accuracy in the exponent and NLL' accuracy in the perturbative expansion of the cumulative distribution. We performed fixed-order calculations at $\mathcal{O}(\alpha_s)$ for global logarithms and $\mathcal{O}(\alpha_s^2)$ for non-global and clustering logarithms, and presented a resummed result valid to all orders. Our $\mathcal{O}(\alpha_s)$ results were found to be consistent with Monte Carlo predictions from the MCFM program.

The distribution exhibits distinct behavior across three key regions of the jet mass variable

1. In the large- ρ region, the distribution is unaffected by trimming.
2. In the intermediate- ρ region, the double logarithms in ρ vanish and are replaced by constant logarithms of $1/z_{\text{cut}}$. Non-global logarithms in this region become leading, significantly influencing the distribution.
3. In the small- ρ region, the double logarithmic structure is restored, and the non-global logarithms converge to those of k_t clustering, characterized by the sub-jet radius R_{sub} . Clustering logarithms appear only in this region, though their numerical impact on the distribution is insignificant.

Following this, we performed a convolution of the resummed form factor, incorporating non-global effects, with the Born cross-section. Our obtained results were compared to parton shower Monte Carlo simulations from `Pythia 8.3`, `Herwig++`, and `Sherpa 2.2` event generators, with non-perturbative effects switched off, yielding reasonable agreement.

While this work focused on obtaining the NLL' resummed distribution, further steps are necessary to make meaningful comparisons with experimental data, such as that provided by the CMS collaboration [19]. Specifically, the inclusion of NLO corrections via matching to fixed-order calculations is required. Moreover, non-perturbative corrections, including contributions from the underlying event and hadronization, are expected to have a significant impact on the distribution [29, 30], and must be included before any comparison with experimental results. These corrections, along with assessments of statistical and systematic uncertainties, will be addressed in our future work.

Acknowledgments

This work is supported by PRFU research project B00L02UN050120230003. We wish to thank the Algerian Ministry of Higher Education and Scientific Research and DGRSDT for financial support. Some of the numerical calculations in this paper have been performed in the High-Performance-Computing cluster at the University of Batna 2 (UB2-HPC). S. Gaid and R. Soualah would like to thank the ICTP for the hospitality, while part of this work was carried out.

A Radiator

The radiator is divided into two contributions, depending on the value of the ρ variable. The total radiator can be expressed as

$$\mathcal{R}_\delta(\rho) = \Theta(\rho - R^2 z_{\text{cut}}) \mathcal{R}_\delta^{\text{ungr}}(\rho, R) + \Theta(R^2 z_{\text{cut}} - \rho) \mathcal{R}_\delta^{\text{trim}}(\rho, R, R_{\text{sub}}, z_{\text{cut}}). \quad (\text{A.1})$$

The ungroomed radiator is given by

$$\mathcal{R}_\delta^{\text{ungr}}(\rho, R) = C_j [L g_1(\lambda) + g_2(\lambda) + g_{2,\text{coll}}(\lambda)] + g_{2,\text{wide}}(\lambda) \sum_{(i\ell)} \mathcal{C}_{i\ell} \mathcal{J}_{i\ell}(R^2), \quad (\text{A.2})$$

where the jet functions $\mathcal{J}_{i\ell}(R^2)$ for the various dipoles are defined in eqs. (3.9a) and (3.9b). The LL and NLL resummation functions are given by

$$g_1(\lambda) = \frac{1}{2\pi\beta_0\lambda} [(1-2\lambda)\ln(1-2\lambda) - 2(1-\lambda)\ln(1-\lambda)], \quad (\text{A.3a})$$

$$g_2(\lambda) = \frac{\beta_1}{2\pi\beta_0^3} \left[\frac{1}{2} \ln^2(1-2\lambda) + \ln(1-2\lambda) - \ln^2(1-\lambda) - 2\ln(1-\lambda) \right] + \frac{K}{4\pi^2\beta_0^2} [2\ln(1-\lambda) - \ln(1-2\lambda)], \quad (\text{A.3b})$$

$$g_{2,\text{coll}}(\lambda) = -B_j \frac{1}{\pi\beta_0} \ln(1-\lambda), \quad (\text{A.3c})$$

$$g_{2,\text{wide}}(\lambda) = -\frac{1}{2\pi\beta_0} \ln(1-2\lambda), \quad (\text{A.3d})$$

where $\lambda = \alpha_s(R^2 p_t^2) \beta_0 L$, and $L = \ln(R^2/\rho)$. The factor K accounts for the transition from the Catani-Marchesini-Webber (CMW) scheme [58] to the $\overline{\text{MS}}$ renormalization scheme

$$K = C_A \left(\frac{67}{18} - \frac{\pi^2}{6} \right) - \frac{5}{9} n_f. \quad (\text{A.4})$$

This result includes the two-loop QCD running coupling effect, such that

$$\alpha_s(k_t^2) = \alpha_s(p_t^2) \left[\frac{1}{1 + 2\alpha_s \beta_0 \ln(k_t/p_t)} - \frac{\beta_1}{\beta_0} \alpha_s \frac{\ln[1 + 2\alpha_s \beta_0 \ln(k_t/p_t)]}{[1 + 2\alpha_s \beta_0 \ln(k_t/p_t)]^2} \right]. \quad (\text{A.5})$$

The one- and two-loop coefficients of the QCD beta function are given by

$$\beta_0 = \frac{11C_A - 2n_f}{12\pi}, \quad (\text{A.6a})$$

$$\beta_1 = \frac{17C_A^2 - 5C_A n_f - 3C_F n_f}{24\pi^2}. \quad (\text{A.6b})$$

The trimmed radiator, which modifies the ungroomed radiator in the intermediate and small- ρ regions, is

$$\begin{aligned} \mathcal{R}_\delta^{\text{trim}}(\rho, R, R_{\text{sub}}, z_{\text{cut}}) = & C_j \left[L g_1^{\text{trim}}(\lambda, \lambda_{\text{sub}}, \lambda_{\text{cut}}) + g_2^{\text{trim}}(\lambda, \lambda_{\text{sub}}, \lambda_{\text{cut}}) + g_{2,\text{coll}}(\lambda) \right] \\ & + g_{2,\text{wide}}(\lambda) \sum_{(i\ell)} \mathcal{C}_{i\ell} \mathcal{J}_{i\ell}(\max[\rho/z_{\text{cut}}, R_{\text{sub}}^2]) + \\ & + g_{2,\text{wide}}(\lambda_{\text{cut}}) \sum_{(i\ell)} \mathcal{C}_{i\ell} [\mathcal{J}_{i\ell}(R^2) - \mathcal{J}_{i\ell}(\max[\rho/z_{\text{cut}}, R_{\text{sub}}^2])], \end{aligned} \quad (\text{A.7})$$

with $\lambda_{\text{cut}} = \alpha_s(R^2 p_t^2) \beta_0 L_{\text{cut}}$, $\lambda_{\text{sub}} = \alpha_s(R^2 p_t^2) \beta_0 L_{\text{sub}}$, $L_{\text{cut}} = \ln(1/z_{\text{cut}})$, and $L_{\text{sub}} = \ln(R_{\text{sub}}^2/\rho)$. The trimming resummation functions are

$$\begin{aligned} g_1^{\text{trim}} = & \frac{1}{2\pi\beta_0\lambda} [(1 - \lambda - \max[\lambda_{\text{cut}}, \lambda_{\text{sub}}]) \ln(1 - \lambda - \max[\lambda_{\text{cut}}, \lambda_{\text{sub}}]) \\ & + (1 - \lambda - 2\lambda_{\text{cut}} + \max(\lambda_{\text{cut}}, \lambda_{\text{sub}})) \ln(1 - \lambda - 2\lambda_{\text{cut}} + \max(\lambda_{\text{cut}}, \lambda_{\text{sub}})) \\ & - 2(1 - \lambda) \ln(1 - \lambda) - (1 - 2\lambda_{\text{cut}}) \ln(1 - 2\lambda_{\text{cut}})], \end{aligned} \quad (\text{A.8a})$$

$$\begin{aligned} g_2^{\text{trim}} = & \frac{K}{4\pi^2\beta_0^2} [-\ln(1 - \lambda - \max[\lambda_{\text{cut}}, \lambda_{\text{sub}}]) - \ln(1 - \lambda - 2\lambda_{\text{cut}} + \max[\lambda_{\text{sub}}, \lambda_{\text{cut}}]) \\ & + 2\ln(1 - \lambda) + \ln(1 - 2\lambda_{\text{cut}})] \\ & + \frac{\beta_1}{2\pi\beta_0^3} \left[\frac{1}{2} \ln^2(1 - \lambda - \max[\lambda_{\text{cut}}, \lambda_{\text{sub}}]) + \frac{1}{2} \ln^2(1 - \lambda - 2\lambda_{\text{cut}} + \max[\lambda_{\text{cut}}, \lambda_{\text{sub}}]) + \right. \\ & + \ln(1 - \lambda - \max[\lambda_{\text{cut}}, \lambda_{\text{sub}}]) + \ln(1 - \lambda - 2\lambda_{\text{cut}} + \max[\lambda_{\text{cut}}, \lambda_{\text{sub}}]) - \ln^2(1 - \lambda) \\ & \left. - 2\ln(1 - \lambda) - \frac{1}{2} \ln^2(1 - 2\lambda_{\text{cut}}) - \ln(1 - 2\lambda_{\text{cut}}) \right]. \end{aligned} \quad (\text{A.8b})$$

Note that the radiator is continuous across the transition points.

The derivatives of the ungroomed and trimmed radiators with respect to L and L_{cut} are given by

$$\frac{\partial \mathcal{R}_\delta^{\text{ungr}}}{\partial L} = \frac{C_j}{\pi \beta_0} [\ln(1 - \lambda) - \ln(1 - 2\lambda)], \quad (\text{A.9a})$$

$$\frac{\partial \mathcal{R}_\delta^{\text{trim}}}{\partial L} = \frac{C_j}{\pi \beta_0} [\ln(1 - \lambda) - \ln(1 - \lambda - \max[\lambda_{\text{sub}}, \lambda_{\text{cut}}])], \quad (\text{A.9b})$$

$$\frac{\partial \mathcal{R}_\delta^{\text{trim}}}{\partial L_{\text{cut}}} = \frac{C_j}{\pi \beta_0} [\ln(1 - 2\lambda_{\text{cut}}) - \ln(1 - \lambda - 2\lambda_{\text{cut}} + \max[\lambda_{\text{cut}}, \lambda_{\text{sub}}])]. \quad (\text{A.9c})$$

Then, the expression for the derivative entering the resummed formula (2.7) is given by

$$\mathcal{R}'_\delta(\rho) \equiv \Theta(\rho - R^2 z_{\text{cut}}) \frac{\partial \mathcal{R}_\delta^{\text{ungr}}}{\partial L} + \Theta(R^2 z_{\text{cut}} - \rho) \left[\frac{\partial \mathcal{R}_\delta^{\text{trim}}}{\partial L} + \frac{\partial \mathcal{R}_\delta^{\text{trim}}}{\partial L_{\text{cut}}} \right]. \quad (\text{A.10})$$

B Clustering functions

The coefficient functions entering the expressions for the CLs factors in eq. (4.22) are given by

$$\gamma(x) = \frac{1}{32\pi} \left[(2x^2 + 1) \sqrt{4x^2 - 1} + 8x^2 (x^2 - 1) \sec^{-1}(2x) \right], \quad (\text{B.1})$$

$$\mu_2(x) = \frac{1}{48\pi} \left[6\sqrt{4x^2 - 1} + 12(2x^2 - 1 - 2\ln x) \sec^{-1}(2x) + 12 \Im \left(\text{Li}_2[-e^{i2 \sec^{-1}(2x)}] \right) \right], \quad (\text{B.2})$$

$$\mu_4(x) = \frac{1}{4} \gamma(x), \quad (\text{B.3})$$

$$\mu_6(x) = \frac{(24x^4 + 2x^2 + 1) \sqrt{4x^2 - 1} + 24x^4 (4x^2 - 3) \sec^{-1}(2x)}{82944\pi}, \quad (\text{B.4})$$

$$\sigma_4(x) = \frac{1}{4} \gamma(x), \quad (\text{B.5})$$

$$\sigma_6(x) = \frac{1}{13824\pi} \left[(6x^4 + x^2 + 2) \sqrt{4x^2 - 1} + 12x^2 (2x^4 - 1) \sec^{-1}(2x) \right], \quad (\text{B.6})$$

$$\tau_6(x) = \frac{1}{110592\pi} \left[(36x^4 - 16x^2 + 7) \sqrt{4x^2 - 1} + 24x^2 (6x^4 - x^2 - 1) \sec^{-1}(2x) \right], \quad (\text{B.7})$$

$$\nu_0(x) = \tau_0(x), \quad (\text{B.8})$$

$$\nu_6(x) = \frac{1}{331776\pi} \left[(12x^4 + 64x^2 + 5) \sqrt{4x^2 - 1} + 24x^2 (2x^4 - 3x^2 - 3) \sec^{-1}(2x) \right]. \quad (\text{B.9})$$

Here, $x > 1/2$. The remaining functions do not have simple analytical expressions and are shown in table 4 for selected values of x .

References

- [1] A. Abdesselam et al., *Boosted Objects: A Probe of Beyond the Standard Model Physics*, *Eur. Phys. J. C* **71** (2011) 1661 [[1012.5412](#)].

x	$\sigma_2(x)$	$\tau_0(x)$	$\tau_2(x)$	$\tau_4(x)$	ν_2	ν_4
0.5	0.0000	0.0000	0.0000	0.0000	0.0000	0.000
0.6	0.00055	0.0017	0.0011	0.00012	0.00011	2.2×10^{-6}
0.7	0.0031	0.0077	0.0057	0.00074	0.00055	0.000020
0.8	0.0087	0.0176	0.0148	0.0022	0.0014	0.000073
0.9	0.0181	0.0305	0.0286	0.0049	0.0026	0.00019
1.0	0.0319	0.0457	0.0475	0.0091	0.0042	0.00039

Table 4. Numerically computed coefficients of the series (4.22) for the k_t CLs factors, evaluated for selected values of $x = R_{\text{sub}}/R$.

- [2] A. Altheimer et al., *Jet Substructure at the Tevatron and LHC: New Results, New Tools, New Benchmarks*, *J. Phys. G* **39** (2012) 063001 [[1201.0008](#)].
- [3] A. Altheimer et al., *Boosted Objects and Jet Substructure at the LHC. Report of BOOST2012, held at IFIC Valencia, 23rd-27th of July 2012*, *Eur. Phys. J. C* **74** (2014) 2792 [[1311.2708](#)].
- [4] D. Adams et al., *Towards an Understanding of the Correlations in Jet Substructure*, *Eur. Phys. J. C* **75** (2015) 409 [[1504.00679](#)].
- [5] CMS collaboration, *Search for massive resonances in dijet systems containing jets tagged as W or Z boson decays in pp collisions at $\sqrt{s} = 8$ TeV*, *JHEP* **08** (2014) 173 [[1405.1994](#)].
- [6] CMS collaboration, *Search for new heavy resonances decaying to WW, WZ, ZZ, WH, or ZH boson pairs in the all-jets final state in proton-proton collisions at $s=13$ TeV*, *Phys. Lett. B* **844** (2023) 137813 [[2210.00043](#)].
- [7] ATLAS collaboration, *Search for high-mass diboson resonances with boson-tagged jets in proton-proton collisions at $\sqrt{s} = 8$ TeV with the ATLAS detector*, *JHEP* **12** (2015) 055 [[1506.00962](#)].
- [8] S. Marzani, D. Reichelt, S. Schumann, G. Soyez and V. Theeuwes, *Fitting the Strong Coupling Constant with Soft-Drop Thrust*, *JHEP* **11** (2019) 179 [[1906.10504](#)].
- [9] H.S. Hannesdottir, A. Pathak, M.D. Schwartz and I.W. Stewart, *Prospects for strong coupling measurement at hadron colliders using soft-drop jet mass*, *JHEP* **04** (2023) 087 [[2210.04901](#)].
- [10] D. Krohn, J. Thaler and L.-T. Wang, *Jet Trimming*, *JHEP* **02** (2010) 084 [[0912.1342](#)].
- [11] S.D. Ellis, C.K. Vermilion and J.R. Walsh, *Techniques for improved heavy particle searches with jet substructure*, *Phys. Rev. D* **80** (2009) 051501 [[0903.5081](#)].
- [12] S.D. Ellis, C.K. Vermilion and J.R. Walsh, *Recombination Algorithms and Jet Substructure: Pruning as a Tool for Heavy Particle Searches*, *Phys. Rev. D* **81** (2010) 094023 [[0912.0033](#)].
- [13] J.M. Butterworth, A.R. Davison, M. Rubin and G.P. Salam, *Jet substructure as a new Higgs search channel at the LHC*, *Phys. Rev. Lett.* **100** (2008) 242001 [[0802.2470](#)].
- [14] M. Dasgupta, A. Fregoso, S. Marzani and G.P. Salam, *Towards an understanding of jet substructure*, *JHEP* **09** (2013) 029 [[1307.0007](#)].
- [15] A.J. Larkoski, S. Marzani, G. Soyez and J. Thaler, *Soft Drop*, *JHEP* **05** (2014) 146 [[1402.2657](#)].

- [16] A.J. Larkoski, I. Moult and B. Nachman, *Jet Substructure at the Large Hadron Collider: A Review of Recent Advances in Theory and Machine Learning*, *Phys. Rept.* **841** (2020) 1 [[1709.04464](#)].
- [17] R. Kogler et al., *Jet Substructure at the Large Hadron Collider: Experimental Review*, *Rev. Mod. Phys.* **91** (2019) 045003 [[1803.06991](#)].
- [18] S. Marzani, G. Soyez and M. Spannowsky, *Looking inside jets: an introduction to jet substructure and boosted-object phenomenology*, vol. 958, Springer (2019), [10.1007/978-3-030-15709-8](#), [[1901.10342](#)].
- [19] CMS collaboration, *Studies of Jet Mass in Dijet and $W/Z + \text{Jet}$ Events*, *JHEP* **05** (2013) 090 [[1303.4811](#)].
- [20] CMS collaboration, *Measurement of the jet mass in highly boosted $t\bar{t}$ events from pp collisions at $\sqrt{s} = 8 \text{ TeV}$* , *Eur. Phys. J. C* **77** (2017) 467 [[1703.06330](#)].
- [21] CMS collaboration, *Measurements of the differential jet cross section as a function of the jet mass in dijet events from proton-proton collisions at $\sqrt{s} = 13 \text{ TeV}$* , *JHEP* **11** (2018) 113 [[1807.05974](#)].
- [22] CMS collaboration, *Study of quark and gluon jet substructure in $Z + \text{jet}$ and dijet events from pp collisions*, *JHEP* **01** (2022) 188 [[2109.03340](#)].
- [23] ATLAS collaboration, *Performance of jet substructure techniques for large- R jets in proton-proton collisions at $\sqrt{s} = 7 \text{ TeV}$ using the ATLAS detector*, *JHEP* **09** (2013) 076 [[1306.4945](#)].
- [24] ATLAS collaboration, *Measurement of the Soft-Drop Jet Mass in pp Collisions at $\sqrt{s} = 13 \text{ TeV}$ with the ATLAS Detector*, *Phys. Rev. Lett.* **121** (2018) 092001 [[1711.08341](#)].
- [25] ATLAS collaboration, *Measurement of soft-drop jet observables in pp collisions with the ATLAS detector at $\sqrt{s} = 13 \text{ TeV}$* , *Phys. Rev. D* **101** (2020) 052007 [[1912.09837](#)].
- [26] M. Cacciari, G.P. Salam and G. Soyez, *The anti- k_t jet clustering algorithm*, *JHEP* **04** (2008) 063 [[0802.1189](#)].
- [27] S. Catani, Y.L. Dokshitzer, M. Seymour and B. Webber, *Longitudinally invariant K_t clustering algorithms for hadron hadron collisions*, *Nucl. Phys. B* **406** (1993) 187.
- [28] S.D. Ellis and D.E. Soper, *Successive combination jet algorithm for hadron collisions*, *Phys. Rev. D* **48** (1993) 3160 [[hep-ph/9305266](#)].
- [29] M. Dasgupta, K. Khelifa-Kerfa, S. Marzani and M. Spannowsky, *On jet mass distributions in $Z + \text{jet}$ and dijet processes at the LHC*, *JHEP* **10** (2012) 126 [[1207.1640](#)].
- [30] N. Ziani, K. Khelifa-Kerfa and Y. Delenda, *Jet mass distribution in Higgs/vector boson + jet events at hadron colliders with k_t clustering*, *Eur. Phys. J. C* **81** (2021) 570 [[2104.11060](#)].
- [31] M. Dasgupta, A. Fregoso, S. Marzani and A. Powling, *Jet substructure with analytical methods*, *Eur. Phys. J. C* **73** (2013) 2623 [[1307.0013](#)].
- [32] M. Dasgupta and G.P. Salam, *Resummation of nonglobal QCD observables*, *Phys. Lett. B* **512** (2001) 323 [[hep-ph/0104277](#)].
- [33] M. Dasgupta and G.P. Salam, *Accounting for coherence in interjet $E(t)$ flow: A Case study*, *JHEP* **03** (2002) 017 [[hep-ph/0203009](#)].
- [34] A. Banfi and M. Dasgupta, *Problems in resumming interjet energy flows with k_t clustering*, *Phys. Lett. B* **628** (2005) 49 [[hep-ph/0508159](#)].

- [35] Y. Delenda, R. Appleby, M. Dasgupta and A. Banfi, *On QCD resummation with $k(t)$ clustering*, *JHEP* **12** (2006) 044 [[hep-ph/0610242](#)].
- [36] S. Marzani, L. Schunk and G. Soyez, *A study of jet mass distributions with grooming*, *JHEP* **07** (2017) 132 [[1704.02210](#)].
- [37] S. Marzani, L. Schunk and G. Soyez, *The jet mass distribution after Soft Drop*, *Eur. Phys. J. C* **78** (2018) 96 [[1712.05105](#)].
- [38] Z.-B. Kang, K. Lee, X. Liu and F. Ringer, *Soft drop groomed jet angularities at the LHC*, *Phys. Lett. B* **793** (2019) 41 [[1811.06983](#)].
- [39] D. Anderle, M. Dasgupta, B.K. El-Menoufi, J. Helliwell and M. Guzzi, *Groomed jet mass as a direct probe of collinear parton dynamics*, *Eur. Phys. J. C* **80** (2020) 827 [[2007.10355](#)].
- [40] S. Caletti, O. Fedkevych, S. Marzani, D. Reichelt, S. Schumann, G. Soyez et al., *Jet angularities in Z +jet production at the LHC*, *JHEP* **07** (2021) 076 [[2104.06920](#)].
- [41] D. Reichelt, S. Caletti, O. Fedkevych, S. Marzani, S. Schumann and G. Soyez, *Phenomenology of jet angularities at the LHC*, *JHEP* **03** (2022) 131 [[2112.09545](#)].
- [42] M. Dasgupta, B.K. El-Menoufi and J. Helliwell, *QCD resummation for groomed jet observables at NNLL+NLO*, *JHEP* **01** (2023) 045 [[2211.03820](#)].
- [43] J. Campbell and T. Neumann, *Precision Phenomenology with MCFM*, *JHEP* **12** (2019) 034 [[1909.09117](#)].
- [44] A. Banfi, G.P. Salam and G. Zanderighi, *Phenomenology of event shapes at hadron colliders*, *JHEP* **06** (2010) 038 [[1001.4082](#)].
- [45] F. Maltoni and T. Stelzer, *MadEvent: Automatic event generation with MadGraph*, *JHEP* **02** (2003) 027 [[hep-ph/0208156](#)].
- [46] J. Alwall, R. Frederix, S. Frixione, V. Hirschi, F. Maltoni, O. Mattelaer et al., *The automated computation of tree-level and next-to-leading order differential cross sections, and their matching to parton shower simulations*, *JHEP* **07** (2014) 079 [[1405.0301](#)].
- [47] C. Bierlich et al., *A comprehensive guide to the physics and usage of PYTHIA 8.3*, *SciPost Phys. Codeb.* **2022** (2022) 8 [[2203.11601](#)].
- [48] J. Alwall, S. de Visscher and F. Maltoni, *QCD radiation in the production of heavy colored particles at the LHC*, *JHEP* **02** (2009) 017 [[0810.5350](#)].
- [49] M. Bahr et al., *Herwig++ Physics and Manual*, *Eur. Phys. J. C* **58** (2008) 639 [[0803.0883](#)].
- [50] J. Bellm et al., *Herwig 7.0/Herwig++ 3.0 release note*, *Eur. Phys. J. C* **76** (2016) 196 [[1512.01178](#)].
- [51] SHERPA collaboration, *Event Generation with Sherpa 2.2*, *SciPost Phys.* **7** (2019) 034 [[1905.09127](#)].
- [52] A. Banfi, G.P. Salam and G. Zanderighi, *Principles of general final-state resummation and automated implementation*, *JHEP* **03** (2005) 073 [[hep-ph/0407286](#)].
- [53] P. Sun, B. Yan, C.P. Yuan and F. Yuan, *Resummation of High Order Corrections in Z Boson Plus Jet Production at the LHC*, *Phys. Rev. D* **100** (2019) 054032 [[1810.03804](#)].
- [54] M. Wobisch and T. Wengler, *Hadronization corrections to jet cross-sections in deep inelastic scattering*, in *Workshop on Monte Carlo Generators for HERA Physics (Plenary Starting Meeting)*, pp. 270–279, 4, 1998 [[hep-ph/9907280](#)].

- [55] A. Buckley, J. Ferrando, S. Lloyd, K. Nordström, B. Page, M. Rüfenacht et al., *LHAPDF6: parton density access in the LHC precision era*, *Eur. Phys. J. C* **75** (2015) 132 [[1412.7420](#)].
- [56] E. Conte, B. Fuks and G. Serret, *MadAnalysis 5, A User-Friendly Framework for Collider Phenomenology*, *Comput. Phys. Commun.* **184** (2013) 222 [[1206.1599](#)].
- [57] M. Cacciari, G.P. Salam and G. Soyez, *FastJet User Manual*, *Eur. Phys. J. C* **72** (2012) 1896 [[1111.6097](#)].
- [58] S. Catani, B.R. Webber and G. Marchesini, *QCD coherent branching and semiinclusive processes at large x* , *Nucl. Phys. B* **349** (1991) 635.